UNIVERSIDADE
BEIRA INTERIOR

Numerical Study: The Influence of Front Wing Pressure Distribution on Wheel Wake Aerodynamics

(Versão após defesa)

Daniel Filipe Teixeira Martins

Dissertação para obtenção do Grau de Mestre em
Engenharia Aeronáutica
(Mestrado integrado)

Orientador: Doutor João Patrício Soares Correia
Orientador: Prof. Doutor André Resende Rodrigues da Silva

abril de 2021

Acknowledgements

First and foremost, I would like to thank my supervisor João Correia for his guidance throughout my master's thesis. Although making me find my own path, his tips and input brought a different perspective to many problems, which was crucial to my success. I am also thankful for his insights regarding the world of motorsports, especially on the engineering side of things, as it gave me the opportunity to appreciate the nuances of his profession.

Secondly, I must also thank my co-supervisor Professor André Silva for his support and for helping me find a feasible subject for my thesis. Despite the fact that many other topics were already available, I insisted on developing a thesis related to Formula One and this came to fruition thanks to Professor André.

My thanks extend to a few of my colleagues, in particular Afonso Carvalho for helping me with the literature review and CAD modelling and Daniel Rodrigues who allowed me to use his workstation for about two weeks.

I have been fortunate enough to make this journey alongside a few other MSc students (who happen to be my close friends) with whom I discussed many ideas and theories. Thank you, guys. Finally, I thank my family for their support and, last but definitely not least, a very special thanks to Helena whose irreplaceable presence and care rendered frustrating times bearable. Thank you for everything, I would not have done it without you.

Abstract

The present study focuses on investigating the aerodynamical interaction between a three-element wing and wheel in ground effect, regarding the Formula One regulations change set for 2022 - amongst the changes is the declutter of the front wing, consequently reducing its complexity. This was accomplished by conducting a three-dimensional computational analysis, using a Detached Eddy Simulation approach, on a simplified one-quarter CAD model, built from the ground up following the regulations imposed by the FIA.

The main goal was to examine how changing the front wing pressure distribution affected wheel aerodynamics, which will then influence the feeding process of the underbody, due to their proximity and subsequent flow interaction. This was done by varying the angle of attack of the second flap on the wing. The CFD study was divided into two sections: a flow analysis and a force analysis. On the flow analysis, one focused on determining the location and intensity of flow energy losses; visualizing the flow structures around the wing and wheel; and, where possible, identifying and comprehending the mechanisms behind the observed flow phenomena. On the force analysis, the transient variations of the force coefficients were examined to better understand how the unsteadiness of the vortices influenced the wing's performance.

The flow investigation indicated that the wheel wake structure is significantly influenced by the wing's flap configuration, showing different shapes to the different geometries tested. This is mainly due to the fact that different flap configurations produce different upwash flow fields, leading to a separation point variation on top of the wheel. This variation then affects the downwash observed behind the central region of the wheel, for a vertical plane.

The force investigation showed that the location of the region of instability influences the behaviour of the transient oscillations, regarding the forces acting on the wing: bearing in mind that vortex breakdown occurs near the wing's trailing edge, higher drag force fluctuations are detected, when compared to downforce fluctuations – a shared pattern across the geometries tested.

Keywords

Aerodynamics; Computational Fluid Dynamics; Numerical Study; Formula One; Wheel; Wing; Ground Effect; Turbulence; Vortex; Breakdown; Transient Flow; Detached Eddy Simulation; Spalart-Allmaras; Unsteady.

Content

List of Tables and Figures

Nomenclature

Symbols

c	Wing chord	m
h	Wing ride height	m
P	Pressure	Nm^{-2}
Re	Reynolds number	
t	Timestep	s
y^+	Non-dimensional normal wall distance	
Δt	Non-dimensional timestep	
U	Freestream velocity	m/s
x, y, z	Cartesian coordinates (horizontal, vertical, downstream)	
μ	Molecular viscosity	$kgm^{-1}s^{-1}$
α	Angle of attack	degrees
ν	Kinematic viscosity	m^2s^{-1}
Ω	Non-dimensional vorticity	
ρ	Density	kgm^{-3}

Abbreviations

AOA	Angle of Attack
CAD	Computer Aided Design
CFD	Computational Fluid Dynamics
CFL	Courant–Friedrichs–Lewy
DES	Detached Eddy Simulation
FFT	Fast Fourier Transform
FIA	Federation Internationale de l'Automobile
LES	Large Eddy Simulations
RANS	Reynolds Averaged Navier-Stokes
S-A	Spalart-Allmaras
SRANS	Steady Reynolds Averaged Navier-Stokes
URANS	Unsteady Reynolds Averaged Navier-Stokes

Chapter 1

Introduction

Up until the late 1960's, little use of aerodynamics was made to enhance the cornering speeds of the cars. Prior to this period, the aerodynamic design was limited to the streamlining of the car's body, with a far greater investment and research on engine performance [1]. The first application of inverted wings, thus creating downforce, was made in 1967 by the Chaparral 2F racing car. Its success ensured that from this day forward the use of such devices was a common thing across all teams [2].

The next big breakthrough came in 1977 with the introduction of ground effect [3]. The first car to make use of this was the Lotus 79, with an underbody shaped like an inverted wing which created a venturi channel between the wing's suction and the ground, therefore generating downforce. Additional side skirts were introduced, further enhancing the effect by sealing the air under the car. Over the years improvements were made upon this technique but the increasing number of accidents resulted in the prohibition of such devices, ending with the implementation of a flat bottom in 1989.

Formula One teams started recurring progressively more to advanced procedures, making use of extensive wind tunnel testing and Computational Fluid Dynamics (CFD) analysis, in order to develop their cars. With wind tunnel testing, many iterations can be promptly analysed, but this method has its limitations and is very expensive. Then came CFD, as an alternative to wind tunnel testing, having less limitations regarding the way one studies a flow, although still limited by processing power and accuracy to the real world.

The field of aerodynamics is one of the most important and impactful factors in the modern world of Formula One racing. Nowadays, teams invest a significant amount of their budget on the research and development of aerodynamics, in hopes of achieving considerable performance gains.

The performance of a racing car can be measured by its maximum lateral acceleration, which translates to higher cornering speeds. Lateral acceleration enhancements are achieved using aerodynamic devices, which increase the downforce produced, supplementing the load on the tyres, thus improving the overall grip levels. However, one must not forget that downforce often comes at the cost of drag (and vice-versa). Therefore, it becomes necessary to find a good balance between maximum attainable grip and straight-line speed for a faster lap time.

One of the governing rules of Formula One dictates that all four wheels of the car must be exposed. Such requirement means there is no body one can place about the wheels in order to control what

is already a very complicated flow structure. In addition, the front wheels are accountable for approximately 40% of the total drag of the car [4]. One can therefore conclude that the flow about the front wheels is of extreme significance. The mismanagement of such flow can result in regions of energy loss, having an impact on the aerodynamic performance of all components downstream.

The front wing of a Formula One racing car has a very important role in all of this. Being the first element to encounter the free stream of air, it dictates the shape of the flow around the other components on the car. The front wing is responsible for generating a trailing vortex system, consisting of several co-rotating vortices [5], shed by the endplates, strakes[1] and the central section of the wing. These vortices then control the wake of the front wheels by re-directing it away from the car.

Gaining a better understanding of the wake's behaviour and interaction with the vortices shed by the front wing will hopefully translate into future performance enhancements.

Figure 1 & Figure 2 - Lotus 1966 & Mercedes 2020.

[1] Strakes are vertical elements placed underneath the wing that align the flow and produce vortices, which not only help with wheel wake management, but also in the decouple of different sections of the wing. Furthermore, they also generate additional suction (vortex induced suction) and induce turbulent mixing in the boundary layer, minimizing flow separation.

1.1. Literature Review

Having in mind the many aspects of race car aerodynamics, the following literature review focuses on the fundamental topics involving the study of a front wing trailing edge vortex system, navigating about a wheel:

- Vortical Flow
- Wheel Aerodynamics
- Combined Wing and Wheel Aerodynamics

1.1.1. Vortical Flow

Despite the considerable amount of work, what constitutes a vortex has long been a source of disagreement between researchers. There is still no clear, unanimously accepted definition of a vortex describing its physical characteristics [6].

Previous definitions mention characteristics such as: pressure minimum at the core; closed or spiralling streamlines and a threshold vorticity [6]. One of them was Green [7], proposing a non-rigorous definition stating that a "fluid vortex is a region of concentrated vorticity". Unfortunately, this only roughly describes what really happens in a vortex.

The most widely accepted condition for the identification of a vortex, more specifically, the location of the vortex core was the one made in 1995, by Jeong & Hussain [6]. In their paper, a mathematical condition is proposed based on the Navier-Stokes equations, focussing on the presence of a pressure minimum, originated without the contribution of vortical motion (i.e., unsteady, irrotational straining and viscous terms). Examining the symmetric S and asymmetric Ω components of ∇u, one can obtain the condition mentioned above:

$$S_{ij} = \frac{1}{2}(u_{i,j} + u_{j,i})$$

$$\Omega_{ij} = \frac{1}{2}(u_{i,j} - u_{j,i})$$

Considering the terms which might create a local pressure minimum and ignoring those which are not a consequence of vortical motion, the symmetric part of the gradient in the Navier-Stokes equations is reduced to what is shown below:

$$\Omega_{ik}\Omega_{kj} + S_{ik}S_{kj} = \frac{-1}{\rho}p_{i,j}$$

One can then define a vortex core as a connected region with two negative eigenvalues of $S^2 + \Omega^2$, because the occurrence of a pressure minimum needs two positive eigenvalues of the tensor $p_{i,j}$.

Jeong & Hussain proceeded to evaluate the validity of their proposal in conditions where previous definition mistakenly found a vortex, concluding that the mathematical condition was very

successful in locating a vortex core. Nonetheless, for situations where the presence of a vortex is known, basic definitions are believed to be more appropriate due to their simplicity.

As previously stated, a vortex can be thought of as a region of concentrated vorticity. Vorticity is an extremely important property of the flow and a necessity when it comes to the generation of a vortex. As such, it becomes important to further elaborate on this concept.

The mathematical definition of a vortex describes it as the curl of the velocity vector, physically related to the angular velocity in the flow [8]. Vorticity is generated by the viscous forces acting near the surface [7] as a consequence of flow passing over it, in a favourable pressure gradient. When the flow separates from the surface in an adverse pressure gradient, the vorticity is transported away from the surface. One can therefore interpret vortices as structures formed due to the rolling up of this separation surface [9].

In 1997, Peckham & Atkinson [10] made early observations regarding vortex breakdown, visualizing the leading edge vortices over a delta wing. At high angles of attack, breakdown can occur instigating a severe loss in lift.

In 1962, Harvey described the phenomenon as “an intermediate stage between the two basic types of rotating flow - those that do and those that do not exhibit axial velocity reversal” [11]. From this definition two consequences can be gathered: vortex breakdown leads not only into an abrupt change in the core’s structure [12] but also a reduction in axial velocity.

Later in 1978, Leibovich proposed a definition, suggesting it is a “disturbance characterised by the formation of an internal stagnation point on the vortex axis, followed by a reverse flow in a region of limited axial extend” [13]. As a matter of fact, the existence of this stagnation point is the commonly accepted characteristic of the breakdown phenomenon [9].

As of today, three different types of vortex breakdown have been observed: Double-Helix, Spiral and Bubble Type [14] and [15]. These observations were made possible by producing a vortex from guide vanes, in a cylindrical tube, utilising dye particles for flow visualization. The different types of breakdown can be obtained varying volume flow rate and swirl.

The Double-Helix breakdown was found to only occur at low volume flow rate, in other words, at low Reynolds Number, by Sarpkaya [14] and Faler & Leibovich [16]. Its applicability is therefore scarce, so it will not be discussed any further.

Increasing the volume flow rate, the Spiral and Bubble type of breakdown occur. The Spiral breakdown is characterised by a rapid deceleration of the flow along the swirl axis, making it prone to stagnation. Shortly after an abrupt twist appears in the core, followed by a spiralling of the flow. After one or two turns the flow ends up breaking down into large-scale turbulence [17].

The Bubble breakdown was characterised by Sarpkaya [14] as a nearly axisymmetric region of reversed flow with a stagnation point. This flow structure was then compared to a body of

revolution placed in the flow [18]. The bubble's interior consists of reversed flow with exchange occurring between the internal and external flow. Further downstream, the core is significantly expanded, observing a spiral-tail at the rear [17].

1.1.2. Wheel Aerodynamics

Although not the case of the present study, as one intends to evaluate the combined wing wheel aerodynamics and their impact on feeding the underbody, it is still important to make some relevant mentions on the matter of isolated wheel studies, with the aim of better understanding wheel aerodynamics.

Concerning the near-wake of an isolated wheel, Mercker and Benerburg [19] named the structures observed to the side of the wheel, where the tyre meets the ground as "jetting vortices". These result from the strong viscous forces in front of the tyre contact patch [20]. The phenomenon, called tyre jetting, happens because the tyre squeezes the flow that becomes stationary in front of it, making the air go around it. The jetting effect occurs only on slick tyres, with grooved tyres not experiencing it. This is explained by the fact that the grooves help connect the high pressure air in front of the wheel, with the low pressure air in the wheel wake, reducing both drag and lift [21].

Additional investigation on the near-wake of an isolated wheel rotating in ground contact was carried out by Robin Knowles [22]. In his study he highlighted the following features as the main characteristics of such a wake:

- A region of velocity deficit in the shape of an inverted-T.
- Large regions of reversed flow exist in both vertical and horizontal sections.
- A trailing vortex system consisting of two contra-rotating vortex pairs, one in the upper half of the wake, and one at ground level.
- All four vortices are centred within, or aligned with, the projected profile of the wheel and have a streamwise axis, thus, do not have a lateral speed component up to one wheel diameter downstream.
- The ground vortex pair are larger, more defined and convected further than the upper vortices.

Robin proposed that just upstream of the contact patch, the convergence of the tyre and road surfaces combine to produce a localised lateral jet on each side of the wheel. The jets deflect the freestream flow as it passes the lower shoulders of the wheel, thus modifying its effective shape. It was this deflection that generated the lower lobes and dragged the observed regions of reversed flow. Previous models of the wheel trailing-vortex system from the literature have been re-visited and revised, resulting in the model seen in Figure 3. Each arrow represents the projection of a streamwise trailing vortex, indicating its size and rotational direction. While previous models were based exclusively on vortex theory, the revised model made use of experimental data as well.

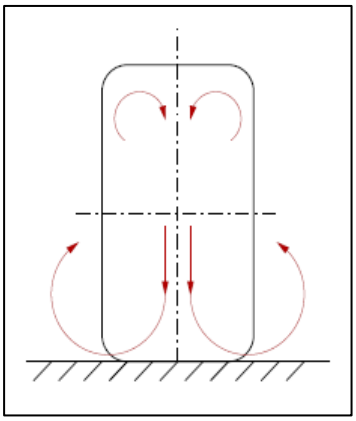

Figure 3 - Revised model of the trailing-vortex system by Knowles.

1.1.3. Combined Wing and Wheel Aerodynamics

Many flow characteristics regarding an isolated inverted wing and a wheel have been described in experimental and numerical studies, yet only a few analysed the interaction between the corresponding flow structures.

A first attempt was made by Kellar et al. [23] using the right-hand quarter of a Formula One racing car in an experimental and numerical study. Although making use of a rotating wheel, the non-consideration of a moving ground, deemed the results not accurate enough. Concerning the numerical analysis, a CFD simulation utilising a coarse mesh of about 340000 cells was put in place.

Diasinos and Gatto [24] studied the effect of the angle of attack and the span of a single element wing on the wake of the wheel, by performing an LDA (Linear Discriminant Analysis). Testing for a Reynolds Number of 5.11×10^4, they observed that the lower wing edge vortex interacted with the wake of the wheel, creating an asymmetric structure. At low wing spans, the vortex travels around the inside of the wheel, while at high wing spans, the opposite occurs. Regarding the angle of attack, observations led to the conclusion that it defined the vortex's size, strength, and degree of movement.

Van der Berg [25] and Van der Berg and Zhang [26] carried out a complete study on the interaction between a double element wing and a wheel. They utilised a non-deformable tyre, similar to what is seen on a Formula One car, at a 2.4° camber[2] to study the impact of ride height and wheel positioning, both experimentally and numerically.

[2] Camber is the angle between the ground and the wheel axis when the wheel is standing flat on the ground.

Placing the wheel behind the wing with a $20\,mm$ gap and overlap, observations were made, concluding the wheel drag was ride height dependent. Compared to an isolated case, ride heights lower than $h/c = 0.3$ saw a lower wheel drag and the opposite occurred for higher ride heights. These effects were discussed and attributed to the delayed separation on top of the wheel, wake interactions and extra suction on the inside of the wheel.

In comparison to the isolated wing case, downforce was higher for lower ride heights and lower for higher ones, while the wing drag increased as ride height was reduced. The primary downforce limiting mechanisms are vortex breakdown and separation, while the channelling effect, allegedly enhanced by wheel rotation, is the primary downforce enhancing mechanism. Changes in wing downforce were attributed to a combination of wheel circulation effect, obstruction by the wheel and dumping effects (when the boundary layer's discharge velocity is increased at the trailing edge, alleviating separation problems by reducing pressure recovery requirements).

The numerical simulations were made using a structured grid of more than 4 million cells with non-conformal zones and applying a RANS simulation with a S-A turbulence model. Wheel drag results could sometimes be underpredicted by more than 25%, while wing results showed a better correlation to the experiments. In using non-conformal zones around the wing, flow features were less accurately predicted.

Bruckner [27] carried out a study on the interaction between a double element wing and a wheel, giving special attention to the transient effects, neglected in previous experiments. These effects are significant, given the wheel's unsteady flow characteristics. A numerical approach using SRANS and DES with additional PIV analysis was made, in order to investigate the effect those components have on each other, varying the ride height.

Simulations using Spalart-Allmaras turbulence model overpredicted the crossflow and incorrectly predicted the wheel's wake downwash. A significant underprediction on wheel drag was also found. In contrast, DES simulations accurately captured all main flow features and more precisely predicted wheel drag.

In comparison to the isolated case, the downforce produced by the wing was smaller for higher ride heights and bigger with less ground clearance. This was attributed to the position of the stagnation point on the wheel, promoting a higher pressure beneath or above the wing, depending on ride height. It was also concluded that at lower ride heights, wheel rotation had no impact on the downforce produced.

Wing position was found to impact the wheel flow structure, observing an increased drag and lift at higher ride heights. At high ride heights the flow is similar to that of an isolated stationary wheel and at lower ride heights it resembles the flow of an isolated rotating wheel. These observations were associated with the circulation induced by the wing and the position of the wing top edge vortex.

The wing lower edge vortex suffers breakdown, as it travels along the wheel at high ride heights. The top edge vortex is diverted upward and inboard by the wheel, showing a lower strength than the one observed in the isolated wing case. This is due to the development of a crossflow between the wing endplate and the wheel.

At lower ride heights, the vortices shed by the lower wheel wake were absorbed by the strong wing lower edge vortex. At higher ride heights, there was a strong fluctuation in wheel drag caused by pressure changes in the lower rear of the wheel. These pressure changes were attributed to the interaction between the upper and lower wheel wake.

Although the study of a combined three element wing and wheel has not been carried out or at least not publicly published, it is still important to mention the improvements a three element wing brings in comparison to a single or a double element wing.

Ramesh K. Agarwal carried out a numerical simulation using RANS equations with SST k-ω turbulence model [28]. Convection terms were discretized using second order upwind scheme. Pressure and velocity were coupled using SIMPLE algorithm. Mesh applied a $y+\approx 1$ with a 300000 cell number, after a mesh independence study. This study found that a three element wing increased the generated downforce by 223% when compared to a single element wing; and by about 50% when compared to a double element wing. In this case, drag was reduced by almost 22% and pressure-to-drag ratio by almost 95%. No results were presented regarding a single element wing.

1.2. Objectives

As previously shown in section 1.1, the wing has a significant impact on the behaviour of the front wheel wake. This flow structure will then affect all aerodynamic devices further downstream, influencing the car's performance on track.

The new aero-regulations, previously set for 2021 then postponed to 2022 due to the global pandemic, aim at reducing the loss of downforce when following another car, through the change of aerodynamic design philosophy. The goal is to implement a set of changes in order to obtain more downforce from the underbody of the car, re-introducing the ground effect, thus relying less on overbody aero devices such as wings.

In the year 2019 the first step towards this goal was made. Front wing designs saw a significant declutter, having less appendices than in previous years (see Figure 4), hence reducing the flow structures.

Up until now, the wing's joint with the neutral section formed a powerful flow structure, named the Y250 vortex (see Figure 5), utilised to clean up the flow to the rear of the car by pushing the wake of the front wheel outboard. In 2022 this will no longer be the case, so the elements will now be connected to the nose (see Figure 6), thus preventing teams from generating said vortex. The

management of the front wheel wake will instead be aided by a deflector placed over the top of the tyre tread. This deflector helps cleaning up the airflow passing over the tyre, fixing the separation point and, consequently, reducing the size of the wake behind the spinning wheel.

Another significant change is with regards to the area in front of the sidepods, where the bargeboards are located. The purpose of these aero devices is essentially to split the airflow arriving from the front of the car into three parts – underfloor, body sides and outwash. This outwash airflow is achieved with the help of guiding vanes that direct the flow outboard, making bargeboards very aerodynamically disruptive for a following car. Therefore, they have been banned from 2022.

Seeing a decrease in over-body aero devices, accompanied by a cleaner wheel wake and lack of complex bargeboards, means that the airflow will not be pushed outside the rear tyres as much, creating a narrower wake behind the car, thus facilitating a following car to get closer and, possibly, overtake.

Having in mind the resources at our disposal, the present work aims at studying the influence of these new front wing designs on wheel wake aerodynamics, which will then severely affect the feeding process of the underbody. This will be accomplished by examining the effects of front wing pressure distribution, through the variation of the angle of attack of the second flap. Defining a set of monitoring points behind the wheel, one is able to access and quantify the total energy of the airflow near the ground and, thus, the effectiveness of the underbody at generating downforce by utilising the ground effect.

The work carried out by Bruckner [27] can be used to validate and support the decisions made in the development of this study, especially on the numerical side of things, given that it paid special attention to the transient effects, validating the DES model for the combined wheel-wing scenario.

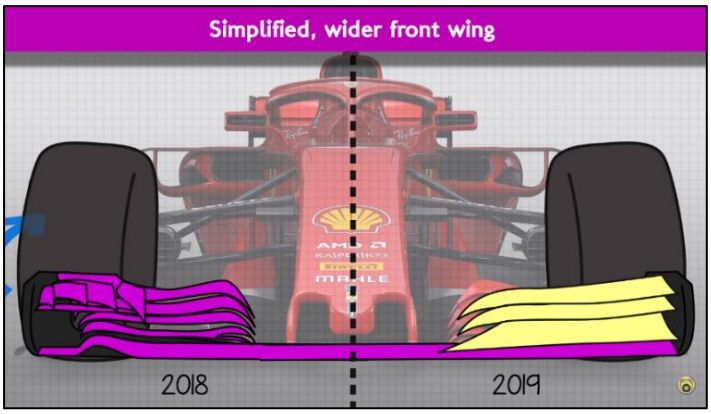

Figure 4 - Front wing: 2018 vs 2019.

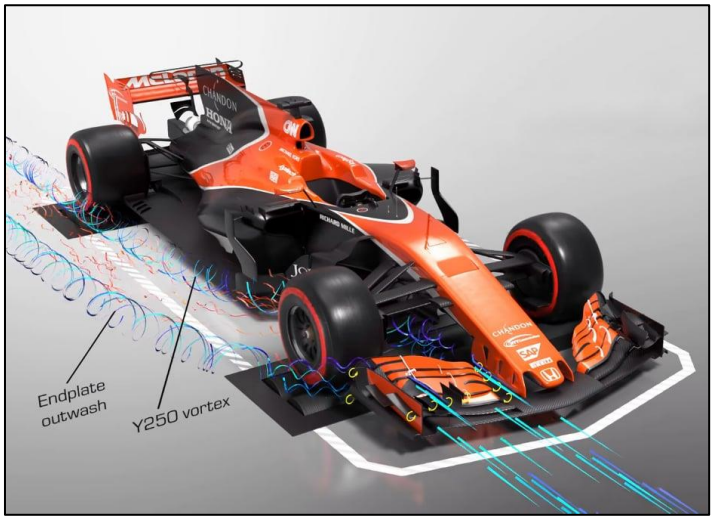

Figure 5 - Illustration of the Y250 vortex.

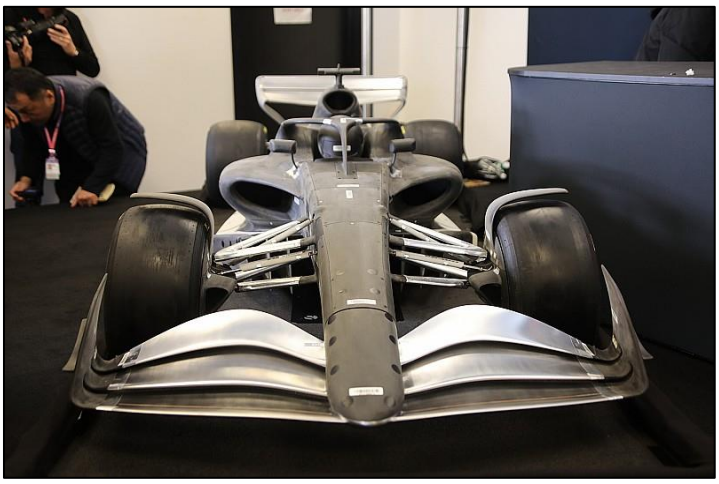
Figure 6 - 2022 Formula One prototype.

Chapter 2

Methodology

2.1. Geometry

It is worth mentioning that the model of the car was made from the ground up, in an attempt to replicate the prototype presented by the FIA, respecting the regulations imposed, where several reference volumes specify the "boundaries" of all relevant components of the car. These "boundaries" can be seen in Figure 7, represented by the outlined, transparent bodies around the model. It is also possible to notice that some simplifications were introduced in order to reduce the computational costs, although never neglecting or compromising the quality of results. Firstly, components such as brake ducts, wheel hubs, tyre deflector, suspension and underbody were not considered. Then, the flow was assumed to be symmetric about the centerspan, an assumption made reasonable by Mahon's study [29], that allowed to only consider half of the car in this study. Moreover, the wheel was modelled so that a contact patch for a wheel camber of 2.4 degrees was considered (see page 59). In accordance with the regulations, cars will use 18 inch wheels, corresponding to a wheel of 720*mm* total diameter and 370*mm* width. The wheel rim is covered and so was the model tested, resulting in no crossflow through the wheel. Wheel hubs are also not represented in order to simplify the flow structure.

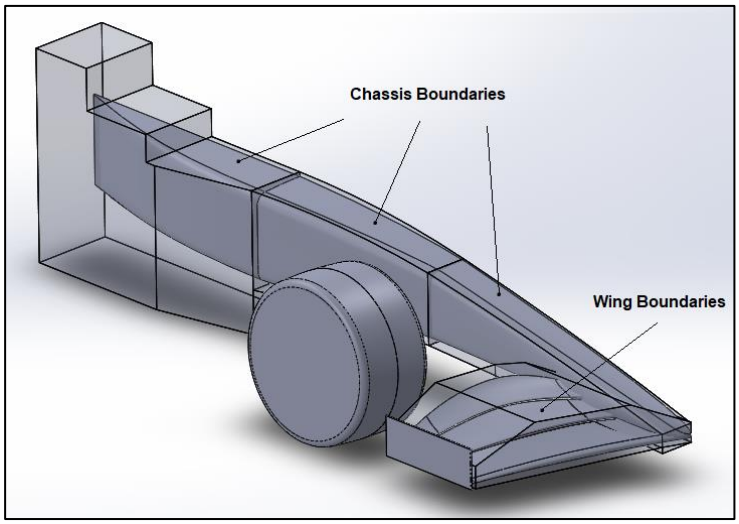

Figure 7 - Geometry overview.

The wing in particular was made relatively similar to the one found on the FIA wind tunnel model and following the 2022 regulations. Starting with a generic profile, several changes were made to best meet the desired geometry. The wing is composed of a main-plate and two individual flaps. Each element on the wing is made out of three profiles - root, mid and tip profile - different to one another. The second flap is the only one that can rotate about an axis (see Figure 8), in order to

reach different AOA, consequently changing the pressure distribution on the wing. This rotation is made possible by two cuts, both perpendicular to the axis, thus ensuring the bodies would not interfere with each other. A summary of the main characteristics of the wing can be found in Table 1. Important to notice that the gap and overlap are almost constant along the span of the wing on each flap and that the angle of attack for flap 2 ranges from 30° to 34°, depending on its configuration. The considerations for measuring the AOA can be seen in Figure 9 and Figure 10.

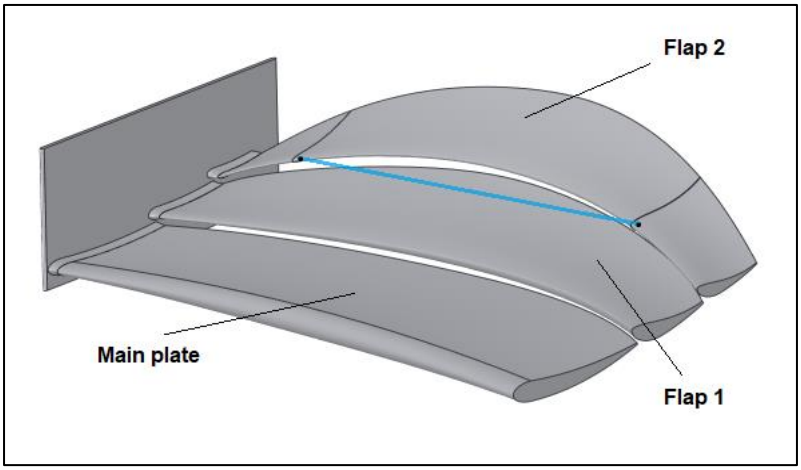

Figure 8 - Wing components (blue line - imaginary axis of rotation).

Table 1 - Wing measurements.

Wing measurements	
Spanwise	800, 786, 770mm
Overlap	~19*mm*
Gap	~12*mm*
Angle of Attack	16°
Main-plate	
Root chord	269.50*mm*
Tip chord	236.58*mm*
Mean chord	253.42*mm*
Angle of attack	0°
First flap	
Root chord	154.72*mm*
Tip chord	141.87*mm*
Mean chord	148.39*mm*
Angle of attack	16°
Second flap	
Root chord	129.00*mm*
Tip chord	96.23*mm*
Mean chord	113.41*mm*
Angle of attack	30°, 32°, 34°

To ensure future reproducibility of the results, the coordinates of each element of the wing are presented in page 65. The task at hand was already vastly demanding and time consuming, so no CFD study was put in place to optimize the wing, aerodynamically speaking. Consequently, undesirable flow phenomena such as vortex bursting may be encountered.

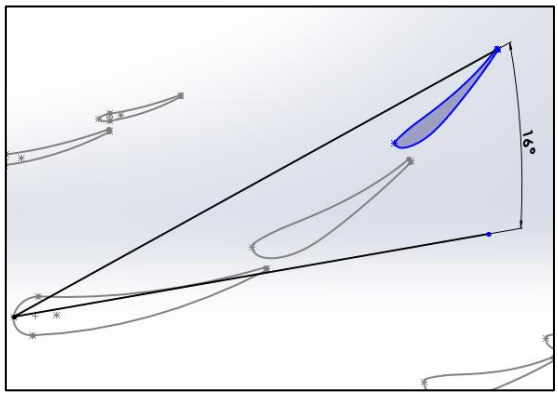

Figure 9 - Flap 1 & 2 AOA for mid profile.

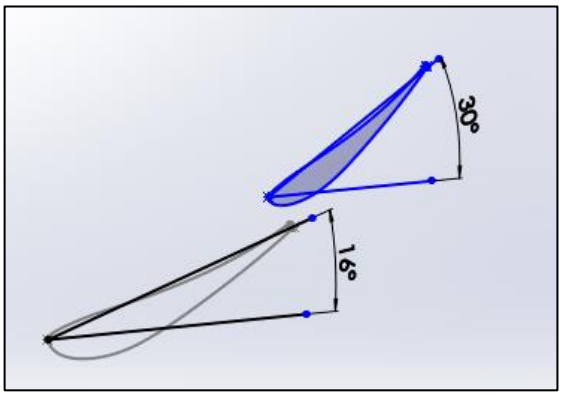

Figure 10 - Wing AOA for mid profile.

2.2. Numerical Approach

This thesis uses a CFD approach to simulate the flow around the car, thus making it important to discuss the numerical setup in greater detail. For a better understanding, the numerical setup can also be described separately in three main stages: the pre-processing stage, the solving stage and, finally, the post-processing stage. To validate the numerical approach, a pressure coefficient study was performed by plotting, and comparing, the theoretical and numerical curves for a generic airfoil. The referred study can be seen in more detail in section 2.3. The software of choice was ANSYS FLUENT, a commercial CFD package used in many different cases, but especially employed in aerodynamical studies. More information can be found in the software user guide [30].

2.2.1. Pre-Processing Stage

- **Computational Domain**

The computational domain needs to ensure its boundaries do not disturb the flow around the car. Regarding the inlet, one needs to guarantee it does not affect the stagnation region and also that it captures the entire extent of the wake. The outlet, on the other hand, cannot affect the recirculation region behind the car. From the available literature, giving special attention to the best practice guidelines [31], and having in mind that the model only encompasses ¼ of the whole car, the computational domain was set at 1.5 car lengths in front of the car and 4.5 car lengths behind it. It is also recommended to pay close attention to the displacement of the model or blockage ratio. This may well have implications on mass continuity due to the fact that a high blockage ratio might induce an artificial acceleration in the flow, causing convergence problems in the solution. Therefore, cross section dimensions were set at 1.5 × 1.5 car lengths, achieving a

displacement no greater than 1.5% in any given cross section. The computational domain (see Figure 11) was generated using *SPACECLAIM* software, available in *ANSYS*. The enclosure is automatically generated by subtracting the geometry of the model to the domain.

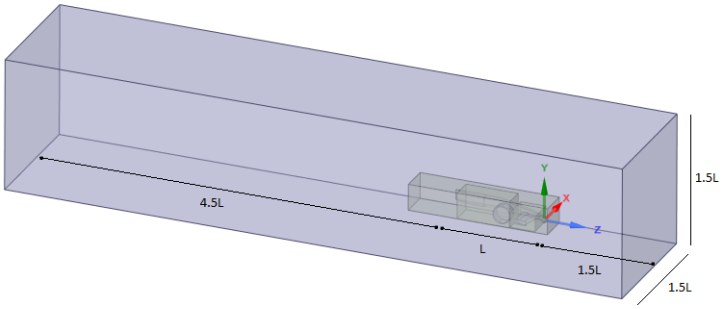

Figure 11 - Computational domain.

- **Bodies of Influence (BOI)**

In order to better control the volume meshing around the car, allowing for a finer mesh and, subsequently, ensuring that flow features such as vortices, are well captured, the so-called bodies of influence (BOI) were employed (see Figure 12). These can be seen as "inner boxes", located inside the computational domain, placed in regions of interest of the car. The first BOI captures the full extent of the model (BOI-All) with a minimum cell size of 1 *mm*, a maximum of 50 *mm* and a growth rate of 1.2; the second was placed around the wing to better capture the boundary layer development on the wing elements (BOI-Wing); and, finally, a third one encloses the area around the wheel, extending further back in order to capture the wake produced (BOI-Wheel). Both BOI-Wheel and BOI-Wing have a minimum cell size of 1 *mm*, a maximum of 15 *mm* and growth rate of 1.2. This area is particularly significant as it dictates the effectiveness of the flow feeding process to the underbody of the car, consequently affecting the total amount of downforce produced and overall performance of the car.

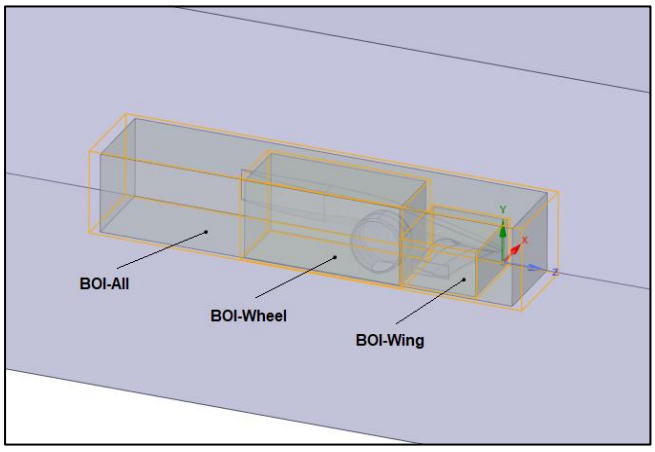

Figure 12 - Bodies of Influence (BOI).

- **Mesh Generation**

"The majority of time spent on a CFD project is usually devoted to successfully generating a mesh for the domain geometry." [32]. This process ensures the model of the car is discretised in order to run the necessary simulations in *ANSYS FLUENT*.

After importing the geometry and making sure all features are present, the first step was to utilise the "Scoped Sizing" feature, where one specifies the mesh characteristics in specific areas. These are the previously mentioned BOI; the wing; the endplate; the chassis; and the wheel.

A mesh independence study (ranging from 6 to 12 million cells) was performed analysing the effects on the values of both lift and drag coefficient. A mesh of approximately 8 million points was considered adequate based on the fact that the force coefficient values did not vary more than 1 to 2% with a higher mesh density. Accordingly, the global parameters for all sizing features were set at a growth rate of 1.2, with a minimum cell size of 1 mm and a maximum of 500 mm to ensure that the geometrical attributes were well captured, and a good cell quality was achieved, while limiting computational costs.

The next step was to write the size field and re-import the geometry alongside it. This allows an automatic remeshing with better quality. Next and making use of the tools present in *ANSYS FLUENT*, one needed to improve the quality parameters of the mesh, giving special attention to the skewness value.

After the tetrahedral mesh was finished, a poly-hexacore mesh needed to be created. This was done using the "Auto Mesh" function. In order to capture and resolve the boundary layer, having also in mind the significance of the y^+ values for the turbulence model in use, one needs to specify the prism layers parameters. The desired y^+ value is determined by the prism layer thickness, more specifically the first cell height. As a result, for a freestream velocity of 50 m/s, aiming at a y^+ value between $1 - 10$ for the surface of the wing, a first layer thickness of 0.05 was obtained. Three individual scoped prism layers were created – one for the wing, one for the wheel and another for the ground. The wing prism layer used a "last-ratio" offset method, with a first cell height of 0.05 mm, 20 layers, the last percent set at 20 and a growth rate of 1.2 (see Figure 13). Ground and wheel prism layers used an "aspect-ratio" offset method, with a first aspect ratio of 3, 3 layers and a growth rate of 1.2.

The final steps before finalising the meshing process include improving the orthogonal quality making use of the "Auto Node Move" feature; scaling down the mesh to meters; prepare for solve; and, finally, switching to "Solution Mode".

It is important to mention that the cells were made concentrated in areas of interest such as the wing, which presents a significant curvature, needing a finer mesh to attain all its nuances, and wake regions. As one moves to regions further away, the cells quickly coarsened (see Figure 14). The mesh was generated using *FLUENT Meshing* software and it can be seen in Figure 15.

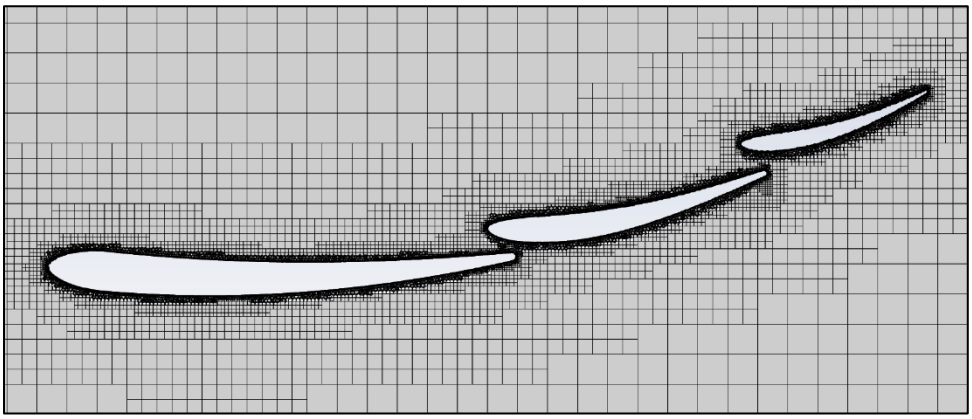

Figure 13 - Grid on the wing. Higher mesh density around the wing to capture the boundary layer.

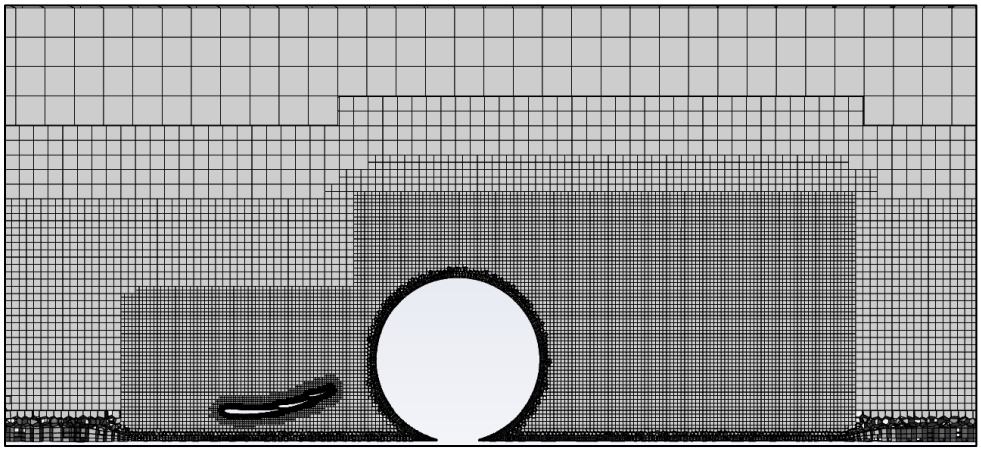

Figure 14 - Side view of the grid for a plane cutting the wing and wheel.

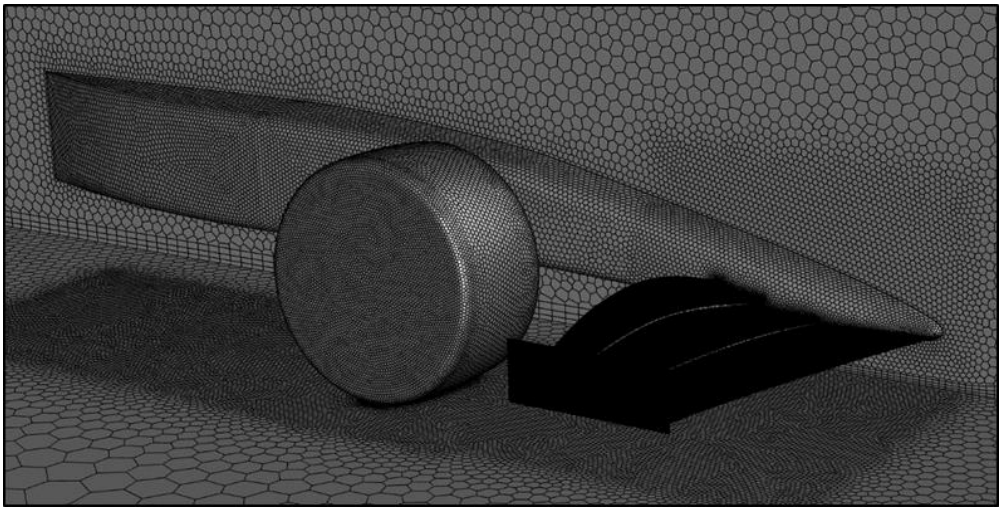

Figure 15 - Mesh (car model, ground, and symmetry wall).

2.2.2. Solving Stage

- **Boundary Conditions**

The upstream boundary was set to "velocity-inlet" with a specified velocity of $50\,m/s$ (equivalent to 180 km/h) which is regulation defined. The downstream boundary was defined as a "pressure-outlet" with a gauge pressure of 0. Turbulence viscosity ratio was set at 5% at the inlet and at 10% at the outlet, reason being the airflow is much calmer at the start and subsequently less turbulent, while at the outlet region, having passed through the full extent of the geometry, the airflow is then more disturbed. This is true even if the outlet is far from the back of the car model. Both air density and viscosity were set to constant values based on ISA.

The symmetry plane was set as "symmetry", equivalent to a specified shear slip of zero. The top and far side walls of the domain were also given the symmetry boundary condition, having in mind that to resolve the wind tunnel boundary layer a much higher grid density had to be applied. The ground was defined as a no-slip moving wall, at $50\,m/s$, which in conjunction with the freestream simulates the flowfield as if the car was the one moving at $50\,m/s$.

The wheel was set as a no-slip rotating wall boundary condition, with an angular velocity of $137.9\,rad/s$, equivalent to a tangential velocity of $50\,m/s$ at the contact patch for an 18 inch wheel. The remaining car surfaces were all set as stationary no-slip wall boundaries.

Freestream velocity of all simulations was set at $50\,m/s$, which corresponds to a chord-based Reynolds Number of 1.37×10^6 based on ISA values ($\rho = 1.225\,kg/m^3$ and $\mu = 1.789 \times 10^{-5}\,kg/ms$).

- **Turbulence Model**

The motion of incompressible fluids can be expressed by the Navier-Stokes equations seen below:

$$\frac{\partial u_i}{\partial x_i} = 0$$

$$\frac{\partial u_i}{\partial t} + U_j \frac{\partial u_i}{\partial x_j} = -\frac{1}{\rho}\frac{\partial p}{\partial x_i} + \nu \frac{\partial^2 u_i}{\partial x_i \partial x_j}$$

where x_i represents the Cartesian coordinates, u_i the velocities and p the static pressure. In more complex flows solving the Navier-Stokes equations directly rapidly becomes too computational expensive. As a result, turbulence models have been created and extensively used in numerical studies.

As previously shown in the literature review, the preferred model for the unsteady flow characteristics of this study is the DES or Detached Eddy Simulation. This hybrid RANS/LES turbulence model is said to combine the efficiency of the RANS approach in the near wall region and the accuracy of LES in the far wall region [33].

Whereas the LES model has a high computational demand, attributed to the fine grid and small timesteps needed to resolve the boundary layer, the DES allows a significant computational cost reduction by having the grid stretched in the direction parallel to the wall surface. This approach uses RANS modelling to resolve the boundary layer, although still capturing the large eddy structures in the far wall regions. The one-equation Spalart-Allmaras model was the chosen one for the RANS modelling. These methods will now be discussed in more detail.

Reynolds-Averaged Navier-Stokes (RANS)

Deriving directly from the Navier-Stokes equations by decomposing them into mean and fluctuating terms, one obtains the Reynolds-Averaged Navier-Stokes equations. In doing so, the pressure and velocity terms can be decomposed as follows:

$$u_i = U_i + \acute{u}_\iota$$

$$p_i = P_i + \acute{p}$$

where U_i and $\acute{u}_\iota$ are the mean and fluctuating terms, respectively. Substituting these terms in the previously stated Navier-Stokes equations one obtains the RANS equations:

$$\frac{\partial U_i}{\partial x_i} = 0$$

$$\frac{\partial U_i}{\partial t} + U_j \frac{\partial U_i}{\partial x_j} = -\frac{1}{\rho}\frac{\partial P}{\partial x_i} + \frac{\partial}{\partial x_j}\left(\nu \frac{\partial U_i}{\partial x_i} - \overline{\acute{u}_\iota \acute{u}_j}\right)$$

These equations have a similar form to the original Navier-Stokes equations, but the variables now represent averages and there are also some additional terms, $-\overline{\acute{u}_\iota \acute{u}_j}$, the Reynolds stresses, representative of the effects of turbulence. From these additional terms arises a closure problem, where the number of equations is insufficient to the existing number of terms. A modelling methodology (i.e., turbulence model) is now needed to close these equations. The level of modelling is related to the number of differential equations added to the Navier-Stokes equations.

Spalart-Allmaras

The Spalart-Allmaras is a one-equation turbulence model, developed specifically for aerospace applications involving wall-bounded flows (aerodynamic flows) [34]. In its original form, this is a low Reynolds number model, which requires the viscosity affected region of the boundary layer to be properly resolved. It has been shown to give good results in boundary layers subjected to adverse pressure gradients.

The Spalart-Allmaras model employs the Boussinesq hypothesis relating the Reynolds stresses to the mean velocity gradients:

$$-\overline{\acute{u}_\iota \acute{u}_J} = 2\nu_t S_{ij}$$

$$S_{ij} = \frac{1}{2}\left(\frac{\partial U_i}{\partial x_i} + \frac{\partial U_i}{\partial x_j}\right)$$

where ν_t is the turbulent kinematic viscosity and S_{ij} is the mean strain rate tensor.

This model solves a single transport equation for the modified turbulent kinematic viscosity:

$$\frac{\partial \tilde{\nu}}{\partial t} + U_i \frac{\partial \tilde{\nu}}{\partial x_i} = C_{b1}\tilde{S}\tilde{\nu} + \frac{1}{\sigma_{\tilde{\nu}}}\left[\frac{\partial}{\partial x_j}\left\{(\nu + \tilde{\nu})\frac{\partial \tilde{\nu}}{\partial x_j}\right\} + C_{b2}\left(\frac{\partial \tilde{\nu}}{\partial x_j}\right)^2\right] - C_{\omega 1} f_\omega \left(\frac{\tilde{\nu}}{d}\right)^2$$

where the turbulent production and destruction terms stand as follows:

$$\tilde{S} = \sqrt{2\Omega_{ij}\Omega_{kj}} + \frac{\tilde{\nu}}{\kappa^2 d^2}\left(1 - \frac{\chi}{1 + \chi f_{\nu 1}}\right)$$

$$\Omega_{ij} = \frac{1}{2}\left(\frac{\partial U_i}{\partial x_j} - \frac{\partial U_j}{\partial x_i}\right) \quad , \quad f_{\nu 1} = \frac{\chi^3}{\chi^3 + C^3{}_{\nu 1}} \quad , \quad \chi \equiv \frac{\tilde{\nu}}{\nu}$$

$$f_\omega = g\left[\frac{1 + C^6{}_{\omega^3}}{g^6 + C^6{}_{\omega^3}}\right]^{1/6} \quad , \quad C_{\omega 1} = \frac{C_{b1}}{\kappa^2} + \frac{1 + C_{b2}}{\sigma_{\tilde{\nu}}}$$

$$g = r + C_{\omega 2}(r^6 - r) \quad , \quad r \equiv \frac{\tilde{\nu}}{\tilde{S}\kappa^2 d^2}$$

$C_{b1}, C_{b2}, C_{\nu 1}, C_{\omega 2}, C_{\omega 3}, \sigma_{\tilde{\nu}}$ and κ are constants, while d is the distance from the closest wall boundary.

$$C_{b1} = 0.1355, C_{b2} = 0.622, C_{\nu 1} = 7.1, C_{\omega 2} = 0.3, C_{\omega 3} = 2.0, \sigma_{\tilde{\nu}} = \frac{1}{2}, \kappa = 0.4187$$

The turbulent kinematic viscosity, ν, can be expressed by the equation seen below, where $f_{\nu 1}$ serves as a viscous damping in the near-wall regions.

$$\nu = \tilde{\nu} f_{\nu 1}$$

The near-wall gradients of the transported variable are much smaller than the ones found in the k-epsilon or k-omega models. Therefore, this model may be less sensitive to numerical errors.

Detached Eddy Simulation

Shur et al. [35] proposed a DES model in which the Spalart-Allmaras turbulence model is used for the unsteady RANS in the near-wall and as the subgrid-scale model for the LES in the far-wall regions. As previously stated, the standard Spalart-Allmaras model uses the distance to the nearest wall as the definition for the length scale d, which plays a major role in determining the level of production and destruction of turbulent viscosity. The DES model replaces d with a new length scale $\tilde{d}$:

$$\tilde{d} = \min(d, C_{des}\Delta_{max}) \quad , \quad C_{des} = 0.65 \quad , \quad \Delta_{max} = (\Delta_{x1}, \Delta_{x2}, \Delta_{x3})$$

where C_{des} is an empirical constant and Δ_{xi} is the grid spacing in the i-th direction, thus meaning the DES resolves the averaged flow field when $d < C_{des}\Delta_{max}$ (unsteady RANS mode) and the filtered flow field when $d > C_{des}\Delta_{max}$ (LES mode).

For a RANS grid with a high aspect ratio in the boundary layer and where the wall-parallel grid spacing usually exceeds δ (boundary layer size), the equation that defines $\tilde{d}$ ensures that the DES model is in the RANS mode. Nevertheless, in a case of grid ambiguity, where $\Delta << \delta$, the DES limiter can activate the LES mode inside the boundary layer, where the grid is not fine enough to withstand resolved turbulence. Therefore, a new formulation of DES, known as the delayed option or DDES [36], is available in ANSYS FLUENT to preserve the RANS mode throughout the boundary layer.

The length scale $\tilde{d}$ is then redefined as follows:

$$\tilde{d} = d - f_d \max(0, d, C_{des}\Delta_{max})$$

- **Solution Procedure**

For all the simulations conducted, a transient, pressure-based solver was used. The flow was initialized using a hybrid initialization and seeing inlet conditions as a reference to compute from.

Concerning solution methods, pressure-velocity coupling was achieved through the coupled algorithm; the interpolation of pressure, momentum and turbulent viscosity used a second-order upwind scheme. As for the transient formulation, the bounded central differencing scheme was used, in accordance with what is recommended for the DES model by the ANSYS software.

One must then select a timestep size that is small enough to resolve time-dependent features, making sure that convergence is achieved within the maximum number of iterations per timestep (following the recommendations for transient flow modelling given by ANSYS, 20 iterations per timestep were stipulated to run the calculations). This means the residuals should reduce around three orders of magnitude (that is drop to 10^{-3}) within each timestep, insuring an accurate resolution of the transient behaviour. To achieve this, one needs to look into the Courant–Friedrichs–Lewy condition (CFL value). This parameter gives a better understanding on how the fluid is moving through the computational domain, taking into consideration minimum mesh size and freestream velocity to obtain a specific timestep size.

$$CFL = \frac{a\Delta_t}{\Delta_x}$$

where a is the freestream velocity, Δ_t is the timestep size and Δ_x is the minimum cell size. Although having an implicit scheme means that the solution is unconditionally stable, regardless of the CFL value, it does not mean an accurate result. A CFL value close to 1 ensures the fluid particles move from one cell to the adjacent other within one timestep, which helps in achieving both convergence and reliable results. In the case of this study, an initial timestep size of $\Delta_t = 2e-05\ s$

was specified. Given the scale of the timestep and the complexity of the case, it would become beneficial to define an adjustable timestep size, as to make the numerical simulation run faster by adapting Δ_t as the calculation proceeds. This decision is reasonable because one is able to increase the CFL value without compromising the results, as long as one ensures it does not exceed a value of $20 - 40$ in the most sensitive transient areas of the domain. Consequently, albeit a lower CFL is required during the first phase of the numerical process, where changes are highly nonlinear, it can be increased as the simulation progresses. Timestep size was increased up to a maximum of $\Delta_t = 2e - 04\ s$.

The flow was allowed to develop until the force coefficients had stabilized, which took around 4000 iterations. From that moment on, statistical data was retrieved using the "data sampling" option provided by the software.

2.2.3. Post-Processing Stage

After the simulations are complete, one can then analyse the results in post-processing. Comparing the three flap configurations - 30°, 32° and 34° AOA – one will try to determine which one optimizes the feeding process of the underbody. This will be achieved by setting the 30° AOA as the base configuration, to which the other two will be compared.

The velocities were non-dimensionalised by the freestream velocity ($U = 50\,m/s$), giving a more comprehensive look at the imagery extracted from FLUENT. Visualizing the behaviour of the flow will be imperative to reach any conclusions about the optimal flap configuration. For this reason, several measurement planes were placed along the length of the CAD model to access the flow development (see Figure 16).

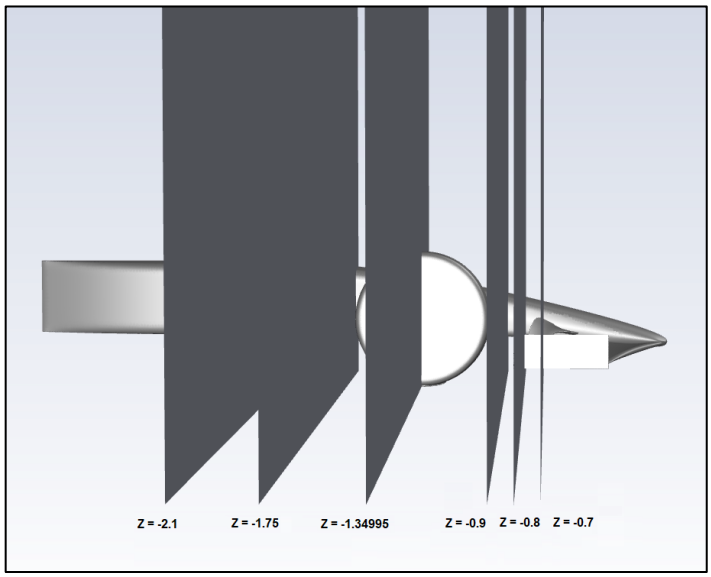

Figure 16 - CFD measurement planes.

2.3. Numerical Validation

The entire geometry was made from the ground up, making this model unique in any way, shape, or form. Therefore, having no direct comparable data, neither experimental nor numerical, verification and validation of the results attained during this study was made difficult. That said, in order to give credibility to this thesis, an experiment was carried out where a generic airfoil was studied under the same numerical approach – mesh parameters, turbulence model, discretization scheme, etc.

The airfoil used was the NACA-2214, with a 14% thickness at 30.03% of the chord length. The objective was to evaluate the pressure coefficient obtained in FLUENT and then compare it to the theoretical value. For that, a rectangular wing was created, measuring 400 mm span and 250 mm chord. Following this, one proceeded to generate a computational domain and respective mesh, being mindful of the parameters previously used when meshing the car's geometry, namely the surface and volume mesh on the wing. A representation of the computational domain and wing's mesh can be seen in Figure 17, where c refers to the wing chord. It is important to mention that the three dimensional effects were not relevant for this analysis and as such, the enclosure goes from root to tip, leaving no space for structures such as wing tip vortices to develop. Concerning the solving stage, a similar setup was put in place to carry a comparable simulation to the ones done on the car.

After the simulations were completed, making use of CFD-POST (a sub-program of ANSYS FLUENT software), a pressure coefficient graph was plotted and then extracted to perform a comparison with the theoretical curve. This curve was obtained using *XFLR5* software, for a NACA 2214 airfoil at an AOA of 0 degrees. The normalized pressure coefficient curves for both cases can be seen in Figure 18. Looking at the graph it is possible to observe that the curves overlap almost perfectly, therefore one can more confidently trust the results obtained concerning the car's geometry and, consequently, verify the validity of the numerical simulations done throughout this study.

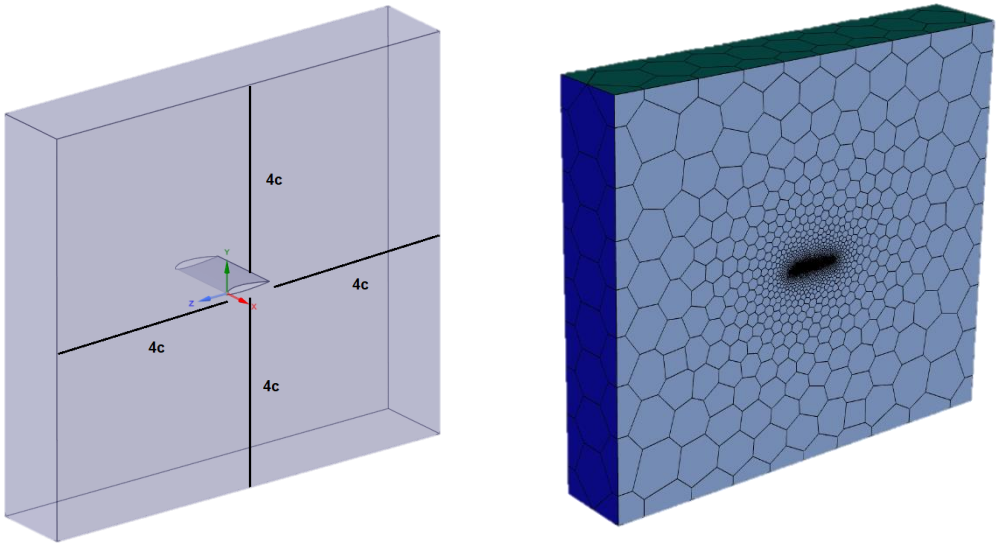

Figure 17 - Computational domain and mesh overview.

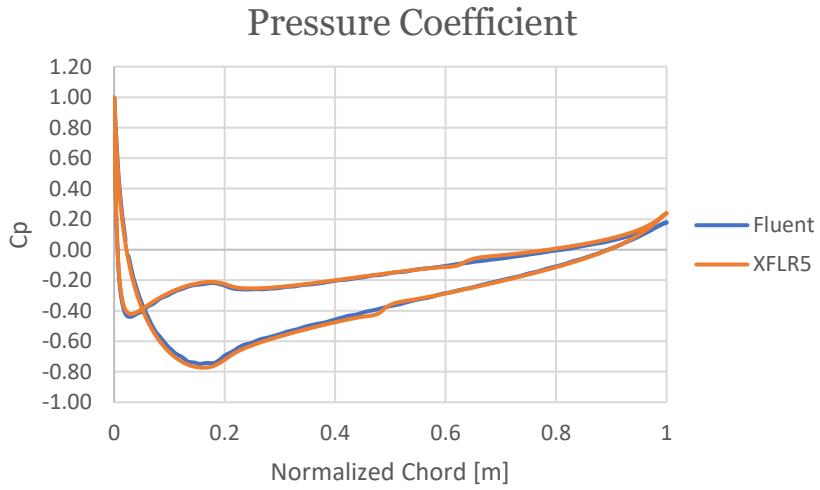

Figure 18 - Pressure coefficient plot for numerical validation.

Chapter 3

Results Discussion

3.1. Residuals

The oscillatory behaviour of the residuals is believed to originate from the vortex shedding which causes a continuous sinusoidal variation in pressure distribution at the trailing edge. Therefore, steady, and continuous oscillations of the residuals are expected.

After analysing the residuals, one can conclude that a good convergence is achieved since the residuals drop by three orders of magnitude within each timestep. This ensures an accurate resolution of the transient behaviour as originally intended. Hypothetically speaking, in the absence of good residual convergence, more emphasis would be placed on the global variables such as the force coefficients, considering the solution converged when the oscillations are within 2 to 5% of the mean value. Even though this was not the case, the coefficient of lift (C_L) and drag (C_D) were chosen as the global variables to help deem the solution converged.

3.2. Flow Analysis

As previously stated, to access and analyse the flow around the car, one has made use of several measurement planes. These planes have been placed in areas of interest normal to the streamwise direction of the wing and where the behaviour of flow structures is most significant to the end goal – feeding the underbody of the car.

In Formula 1 a common process for examining such complex flow structures is done by a total pressure coefficient (C_PT) analysis. This is a non-dimensional parameter which translates the energy of the flow relative to the car. The red areas indicate high energy flow, while the blue areas indicate low energy flow, making it possible to extract some information about how effective the components will be and where there is still high energy flow to play with. The images obtained from CFD regarding C_PT can also give an idea about the presence of vortical structures.

3.2.1. Wing

In addition to generating downforce, the wing's purpose is to shape the flow around the car, having a significant impact on downstream components. Edge vortices are created on the wing as a consequence of the pressure difference between its surfaces. These vortices play an important role on the wing, especially the lower edge vortex being one of the downforce enhancement mechanisms [29]. For that reason, the wing flow structure will now be discussed in more detail.

Analysing the C_PT plots, it is possible to observe two individual vortices originating from the endplate – the upper and the lower vortex – both rotating in an anti-clockwise direction, from the

high to the low pressure regions. Starting small and gaining energy as they travel downstream, these two vortices have different evolution rates. While the upper vortex stays relatively small, the lower edge vortex gets significantly larger as the flow develops.

The differences start to become noticeable at plane $z = -0.7$. This is believed to occur because it is at this plane that the influence of the second flap configuration is felt. For an AOA of 32 degrees, less energy losses are observed, meaning the resulting flow has more energy, when compared to the baseline geometry. This is understood by the smaller size of the lower edge vortex and its lighter blue colouring (see Figure 19). With regards to the 34 degrees geometry, a similar vortical structure is observed when compared to the baseline geometry. Moving downstream, at plane $z = -0.8$, when compared to the other two geometries, the vortex seen for an AOA of 32 degrees is considerably smaller and judging by the colour scale, one can also conclude less energy is lost by the flow (see Figure 20). From this one can deduce that while this vortex is still relatively cohesive, the other two geometries (30 and 34 degrees) see a vortex breakdown starting to occur. However, moving to plane $z = -0.9$, the breakdown of the lower edge vortex is seen beneath the wing in all geometries, observing a wide disturbed structure, which causes recirculation. The baseline geometry exhibits a wider disturbed structure, when compared to the other two, which are of similar dimensions (see Figure 21). This breakdown occurs almost certainly as a consequence of the lower edge vortex produced being too weak to sustain flow development. This will have a major impact on how the wing influences the wheel flow, as only a coherent vortex could significantly affect and laterally contain the wake coming from the wheel. That said, one could try correcting this undesirable phenomenon by creating a stronger lower edge vortex. Understanding that vortices result from the roll up of the airflow as a consequence of a pressure differential, one could either try tilting the main-plate to a more appropriate AOA or shape the airfoil and/or endplate differently, with the goal of reducing the local pressure coefficient, which would also generate more downforce. Concerning vortices, it remains important to mention that the angle of attack has little to no influence on the upper vortex. This is because the pressure increase provided by the stagnation point at the most upstream location of the wheel is greater than that which may be obtained by increasing the angle of attack [37].

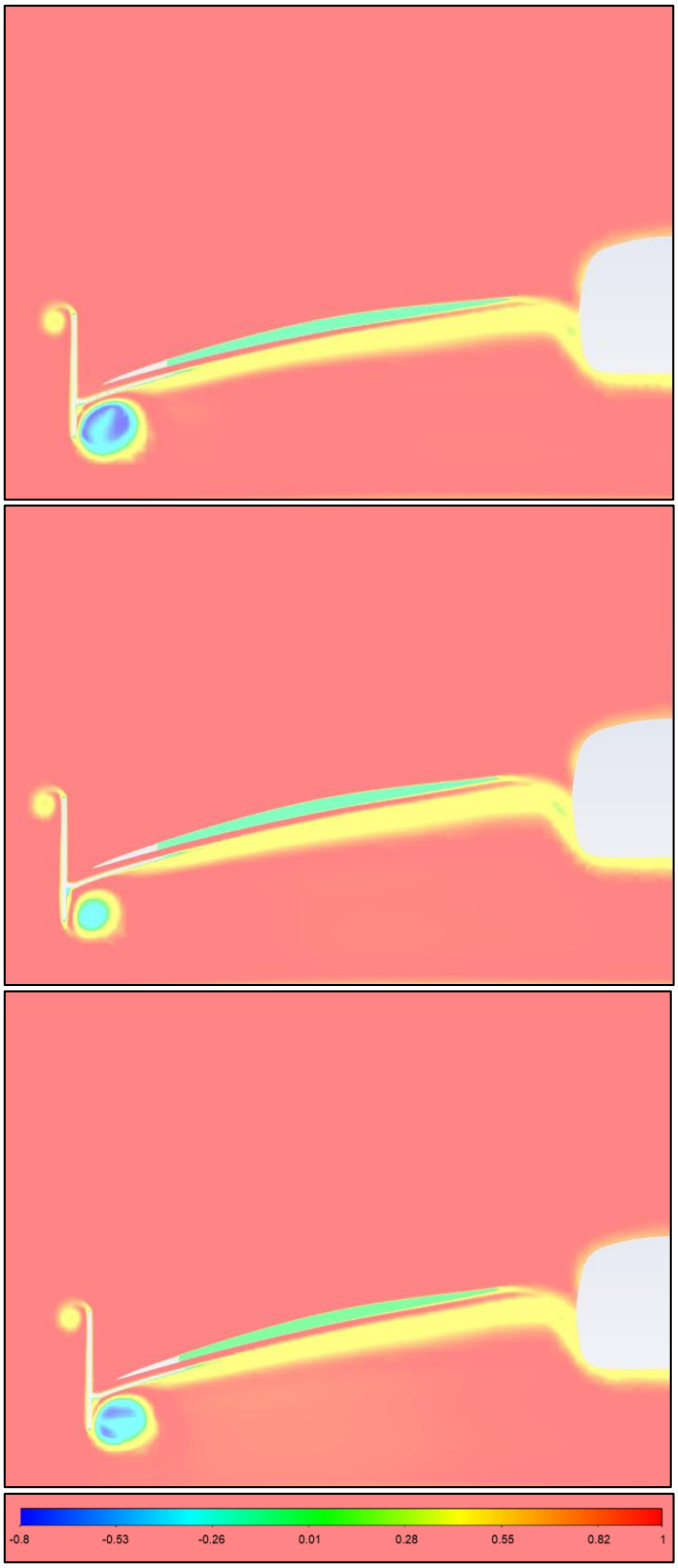

Figure 19 - Total pressure coefficient at plane $z = -0.7$ (AOA of 30, 32 and 34 degrees).

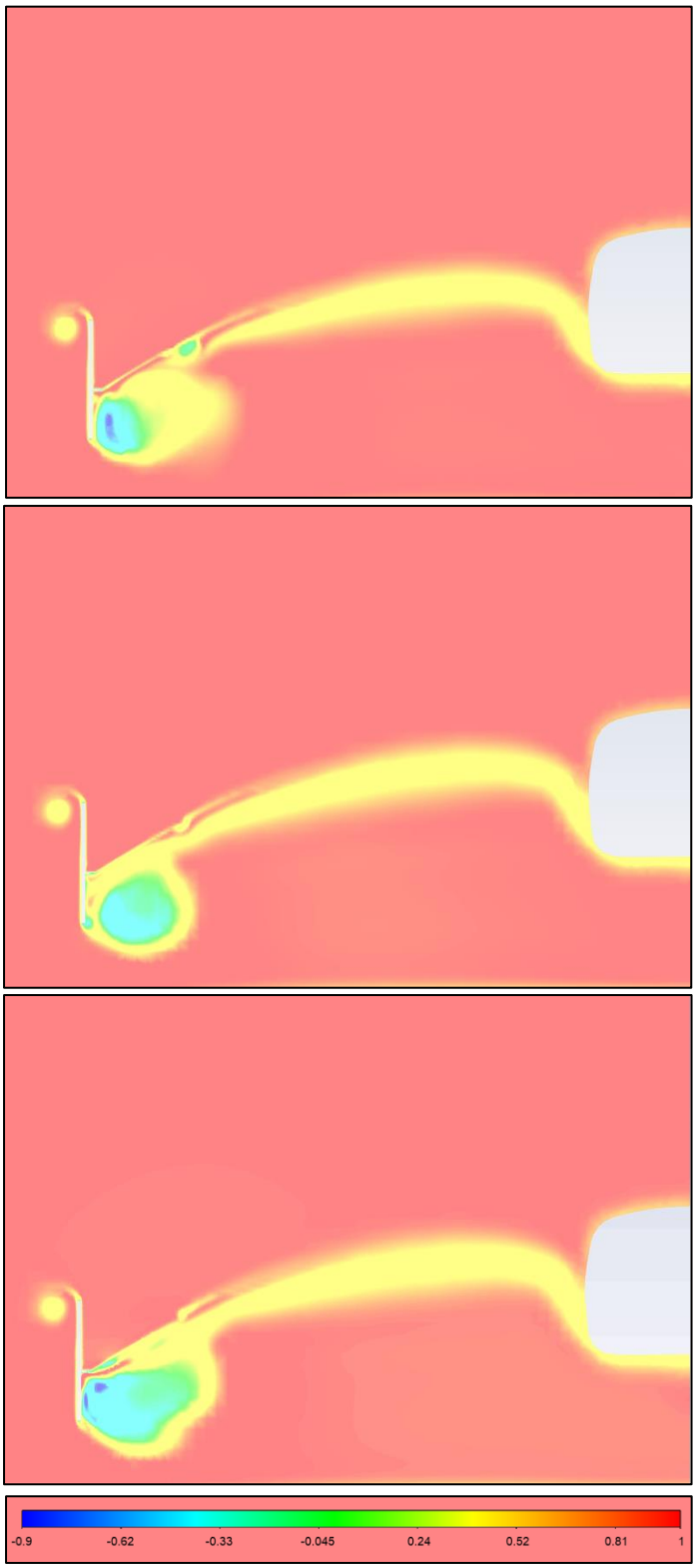

Figure 20 - Total pressure coefficient at plane $z = -0.8$ (AOA of 30, 32 and 34 degrees).

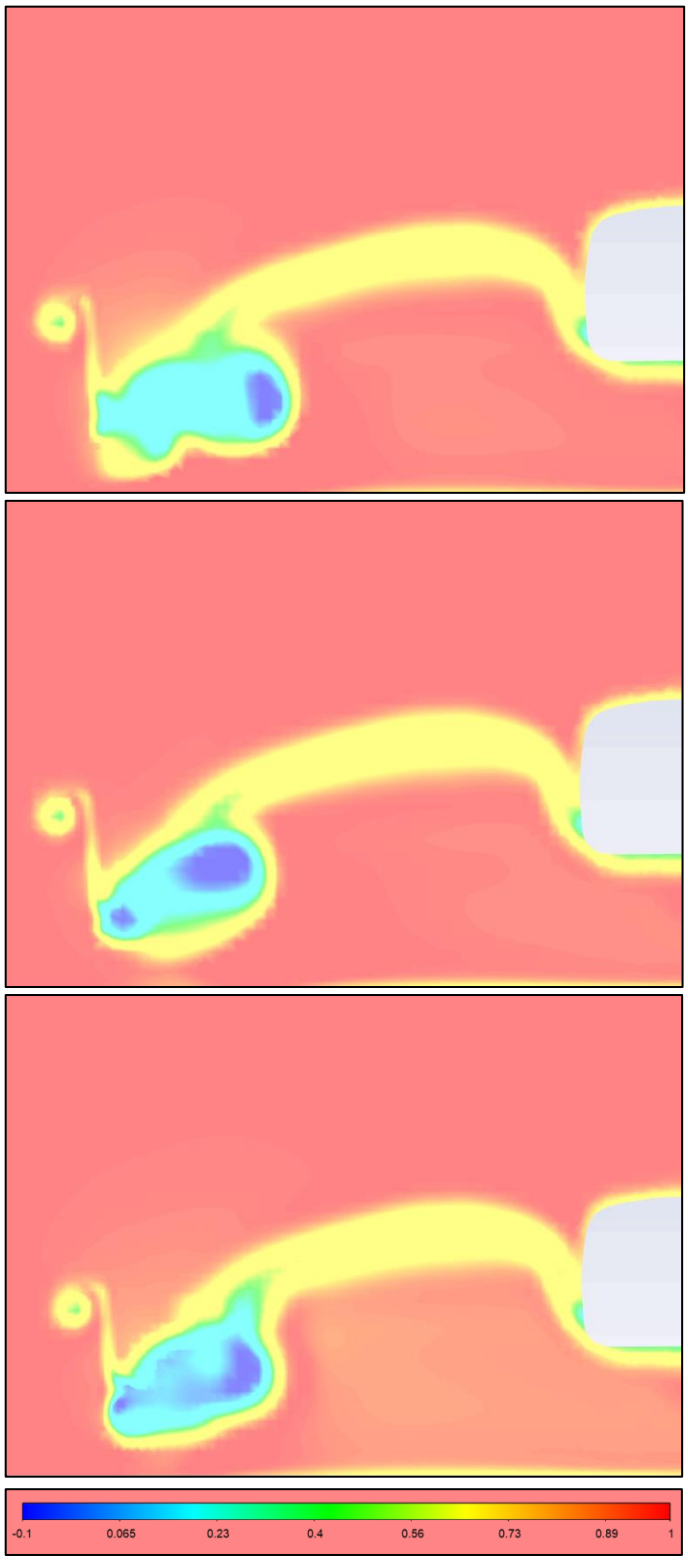

Figure 21 - Total pressure coefficient at plane $z = -0.9$ (AOA of 30, 32 and 34 degrees).

3.2.2. Wheel

Affected by the flow coming from the wing, the wheel aerodynamics will behave differently depending on flap configuration, which will then influence the feeding process of the underbody, due to their proximity. For this reason, the wheel wake aerodynamics will now be investigated.

From the C_PT plots, for a measurement plane placed at $z = -1.34995$ (mid-wheel), it is possible to observe, in all three configurations, a lower turbulent flow to the side of the wheel, where the tyre meets the road (see Figure 22). The phenomenon results from the strong viscous actions in front of the tyre contact patch (jetting effect), as mentioned in the literature review. When compared to the baseline geometry, both the 32 and 34 degrees configurations exhibit a more confined turbulent flow, although the latter is less vertically restrained. Judging by what was seen regarding the lower edge vortex breakdown taking place on the wake of the wing, this is believed to occur because, when compared to the other two configurations, the baseline geometry sees the most disturbed flow succeeding vortex breakdown. As a consequence, its effectiveness on constraining the jetting effect might become impaired.

The wheel wake can be divided into two regions: an upper wake and a lower wake. The lower wheel wake extends further downstream, which is explained by the ground presence and jetting effect [27]. At plane $z = -2.1$, placed where the intake of the underbody would be, the wake coming from the wheel is generally about the same size for both the 30 and 32 degrees configurations. That said, the latter sees the lower wake more to the side, disrupting the area of intake more, leaving less high energy flow to be used by the underbody (see Figure 23). With regards to the 34 degrees configuration, it can be observed a wider but significantly shorter wake structure, which is also located more to the side, closer to the chassis. This structure displays more areas of low energy flow, indicating more energy is lost in comparison to the other two cases.

The streamwise and vertical velocity parameters offer an even better picture about the wake of the wheel. The streamwise velocity displays the velocity deficit caused by the reduced dynamic pressure in the wheel wake, while the vertical shows the change in flow angle, where zero is aligned with the freestream flow, positive is upwash and negative is downwash. Looking at the streamwise velocity at plane $z = -1.75$ (behind the wheel), the wake shows a very similar structure between the 30 and 32 degrees configurations (see Figure 24), both exhibiting areas of strong reversed flow, which are contained within the profile of the tyre. The same cannot be said about the 34 degrees configuration, where the wake is dissimilar, being shorter but wider at ground level, resembling more an inverted-T shape, as observed by Knowles [22]. In this configuration there are no concentrated zones of strong flow reversal, unlike the other two geometries. The explanation for this may reside on the upper wake structure being stronger, which entrains more flow into this region, thus replacing in-wash (reversed flow) with downwash [38]. Further downstream, at plane $z = -2.1$ (underbody's intake), a similar behaviour is observed, the wake structure is again similar between the baseline and the 32 degrees geometry, however the strong reversed flow regions are no longer present (see Figure 25). The containment

of the wake structure within the profile may be the explanation to this lack of advection of the reversed flow downstream of the wheel [38]. Concerning an AOA of 34 degrees, it presents itself shorter but wider, affecting significantly more the feeding process of the underbody.

Regarding the vertical velocity, for a plane $z = -1.75$ (behind the wheel), overall, one can observe a very similar wake structure between the AOA of 32 degrees and the baseline geometries. However, the baseline geometry shows a very small area of downwash in the lower half of the wake, behind the wheel, which is not observed in the 32 degrees configuration (see Figure 26). With regards to the AOA of 34 degrees configuration, the wake is rather different, observing a fairly large area of downwash behind the central region of the wheel. This observation goes to justify what was seen before in the streamwise velocity analysis because, as the separation point moves rearwards, the downwash generated in the central region of the wheel wake increases incrementally, leading to a resultant wheel wake that is closer to the ground (shorter) and more further apart [37]. The delay of the separation point is believed to happen because the more aggressive flap configuration (AOA of 34 degrees) induces more upwash, thus providing the boundary layer with more energy to overcome the adverse pressure region on top of the tyre. This hypothesis can be assessed by tracking the path taken by the flow through the wing and wheel. Analysing Figure 28, which illustrates the pathlines coloured by velocity magnitude, it can be seen that for an AOA of 34 degrees the flow is indeed more deflected upwards by the second flap, which will help move the separation point on top of the wheel rearwards. The increased downwash experienced in the central region of the wheel is also the explanation as to why more areas of low energy flow were seen in Figure 23, regarding the 34 degrees case. In other words, why more drag is produced by the wheel [37]. Figure 29 offers a great representation of the flow behind the wheel, where one can observe it is notably more deflected downwards for an AOA of 34 degrees. Moving downstream at plane $z = -2.1$ (underbody's intake) and comparing the AOA of 32 degrees to the baseline configuration, the wake is again very similar. With respect to the AOA of 34 degrees, an area of downwash is again identified behind the wheel area, as well as a significant region of upwash closer to the chassis, both which are not observed in the other two geometries (see Figure 27). The origin of the referred upwash can be comprehended by observing the pathlines plot (Figure 28), where one concludes that it is a consequence of the deflection imposed by the second flap on the flow coming from the underside of the wing (labelled A).

A change in the wake produced by the wing indicates there will be differences to the surface pressure and forces at play. It now becomes important to analyse and access the forces acting on the wing and their transient behaviour. This will be discussed next.

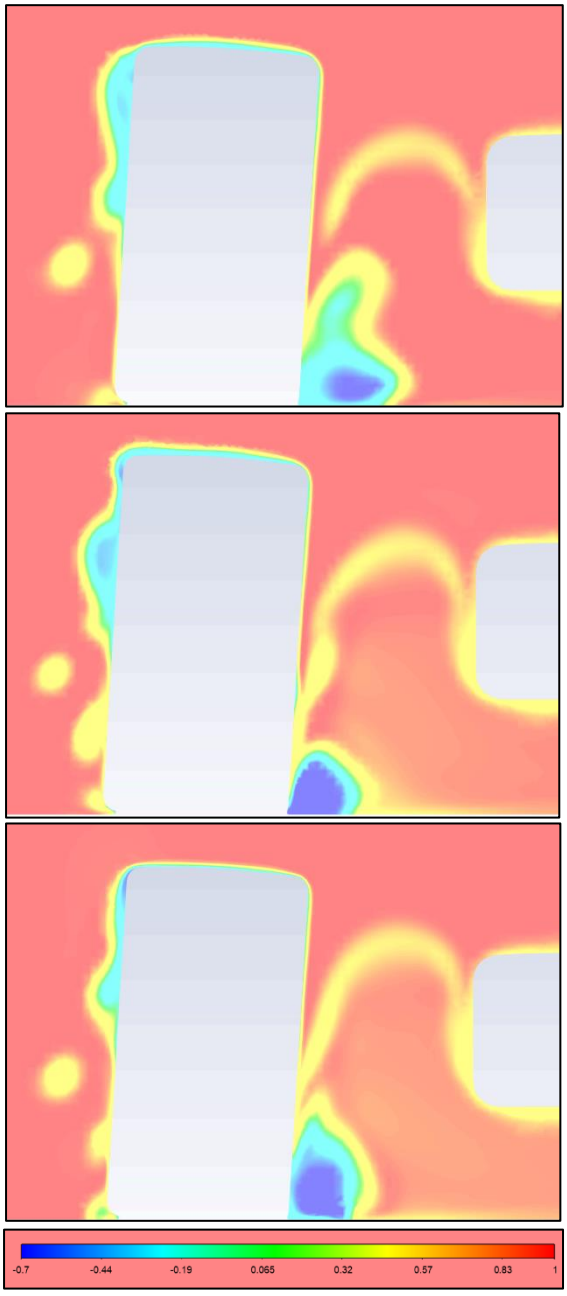

Figure 22 - Total pressure coefficient at plane $z = -1.35$ (mid wheel) (AOA of 30, 32 and 34 degrees).

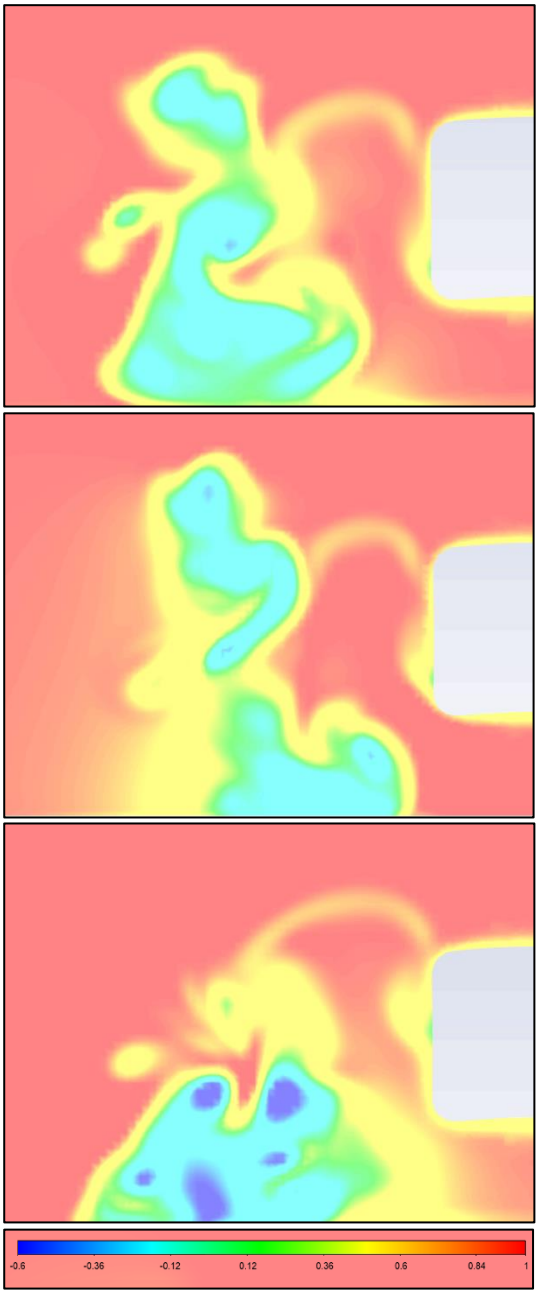

Figure 23 - Total pressure coefficient at plane $z = -2.1$ (underbody) (AOA of 30, 32 and 34 degrees).

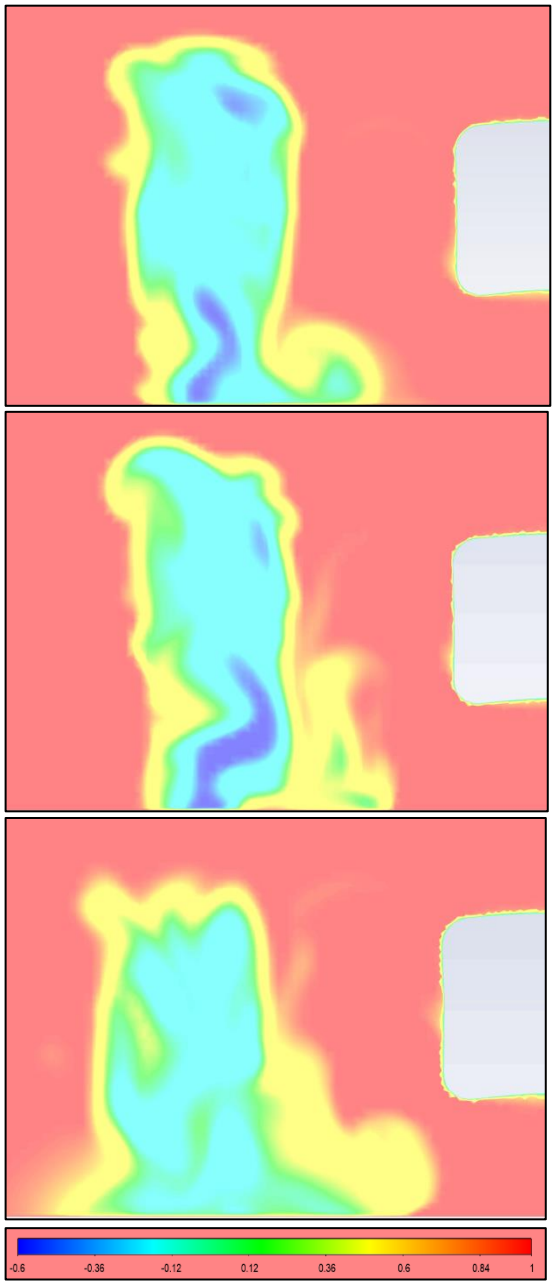

Figure 24 – Streamwise velocity at plane $z = -1.75$ (behind wheel) (AOA of 30, 32 and 34 degrees).

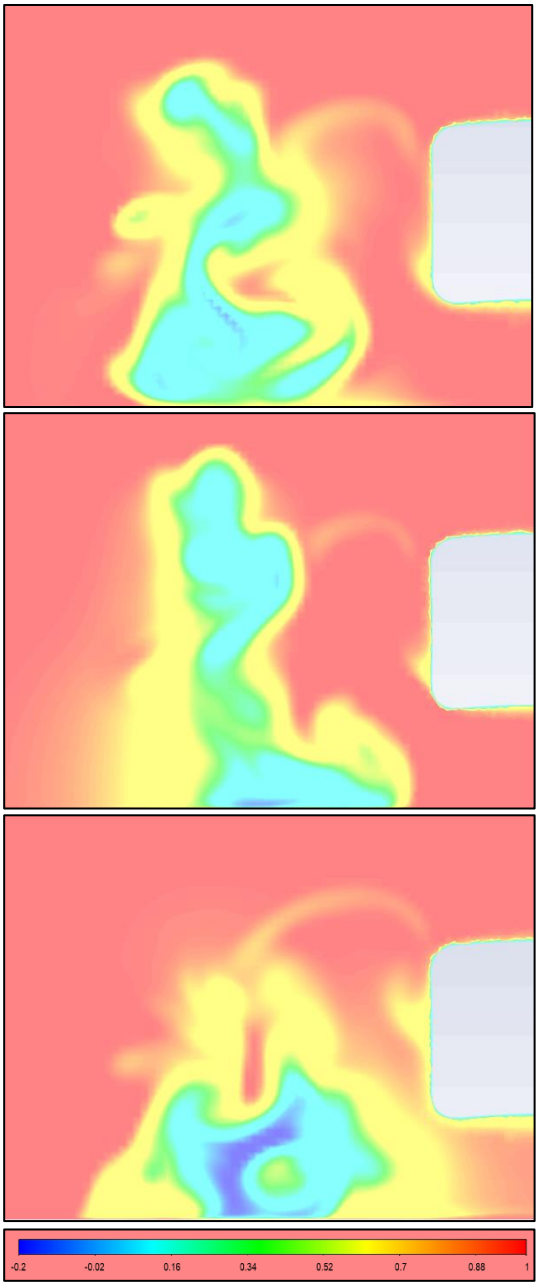

Figure 25 - Streamwise velocity at plane $z = -2.1$ (underbody) (AOA of 30, 32 and 34 degrees).

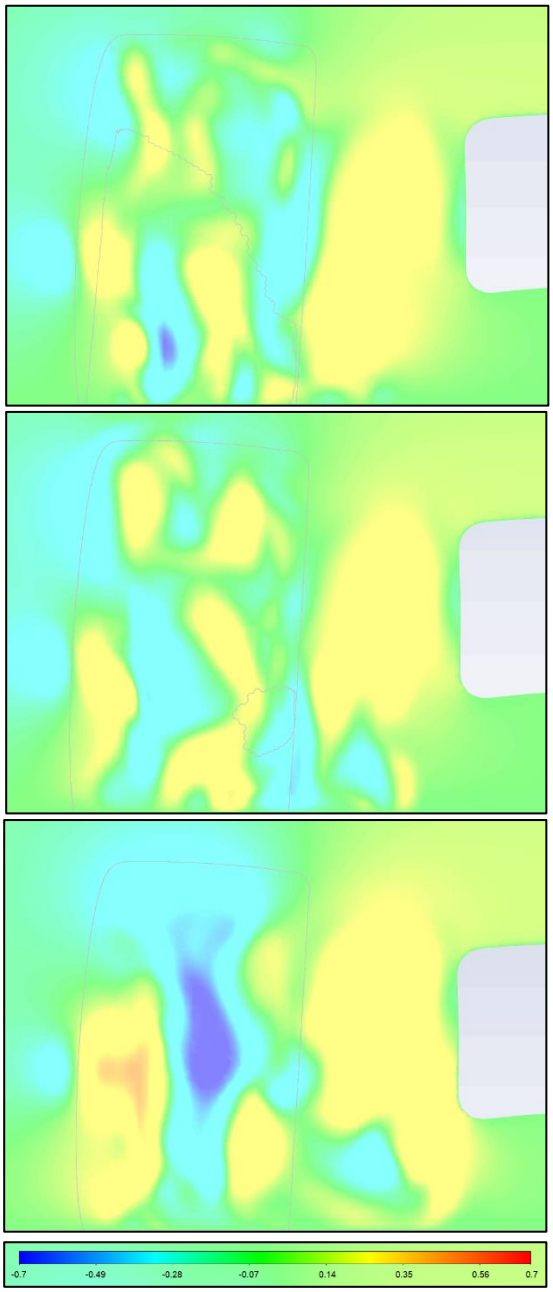

Figure 26 - Vertical velocity at plane $z = -1.75$ (behind wheel) with the outlines of the wheel in light grey (AOA of 30, 32 and 34 degrees).

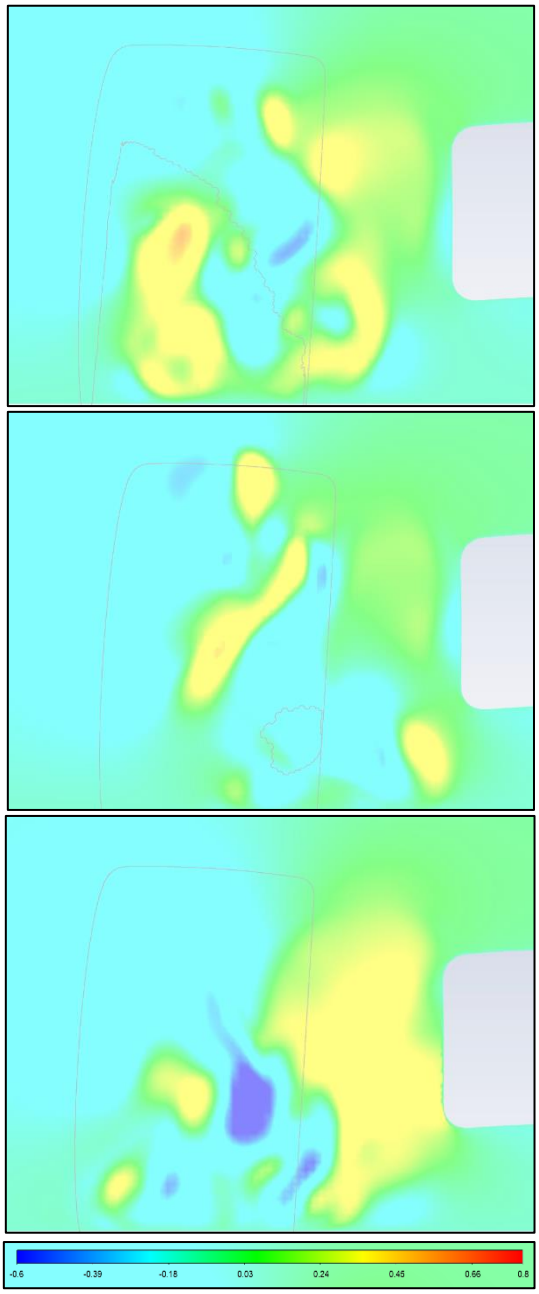

Figure 27 - Vertical velocity at plane $z = -2.1$ (underbody) with the outlines of the wheel in light grey (AOA of 30, 32 and 34 degrees).

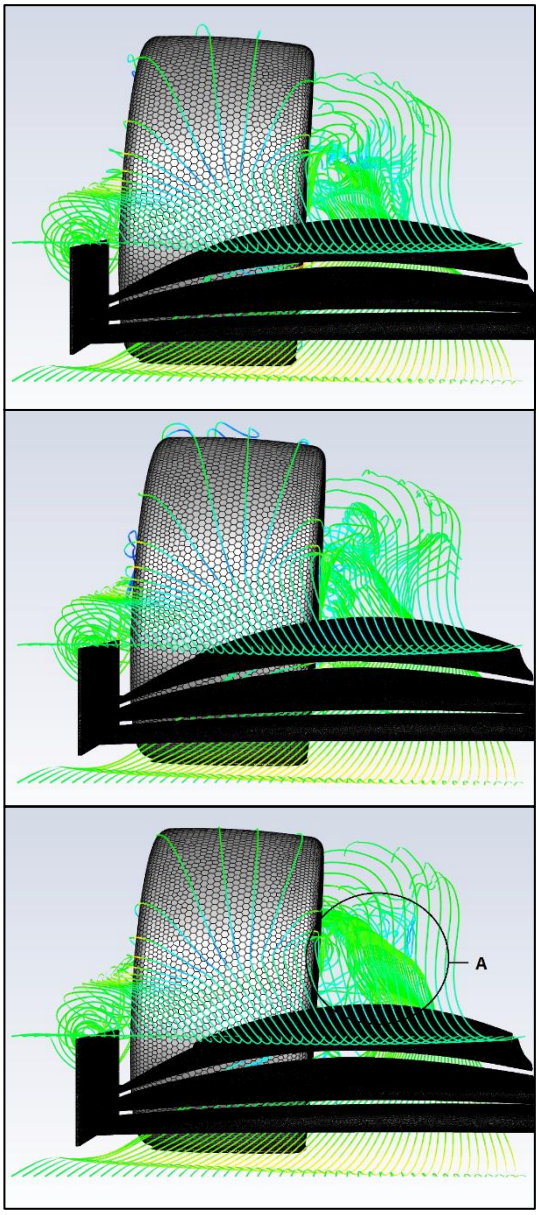

Figure 28 - Pathlines coloured by velocity magnitude (front view for an AOA of 30, 32 and 34 degrees).

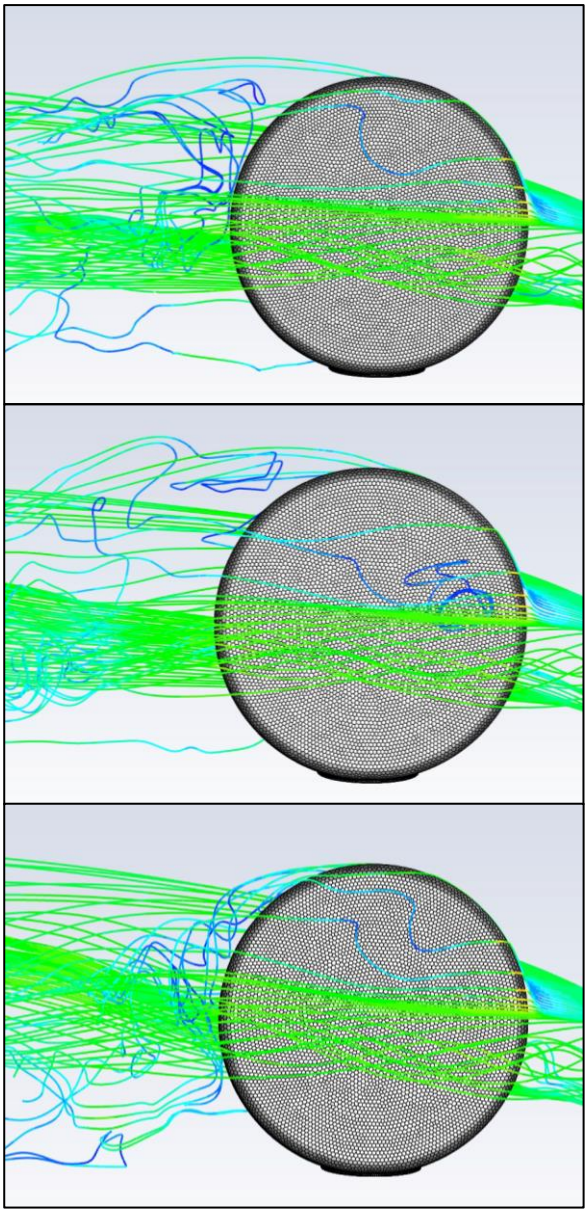

Figure 29 - Pathlines coloured by velocity magnitude (side view for an AOA of 30, 32 and 34 degrees).

3.3. Force Analysis

As one intends to study the flow behaviour near the underbody intake of the car, the forces acting on the wing – lift (C_L) and drag (C_D) – for each flap configuration will now be investigated. It is important to notice that the coefficient of lift is positive in the negative y direction, thus representing the downforce generated by the wing.

When it comes to unsteady simulations, oscillations of the force coefficients are foreseeable. Investigating these transient variations provides a good picture at how the unsteadiness of the lower edge vortex affects the performance of the wing. The oscillations will be examined using a Fast Fourier Transform (FFT) – a mathematical method used to transform a function of time into a function of frequency – useful when analysing time-dependent phenomena such as this study. The resulting plot allows one to inspect if there is any dominant frequency. This was done using *MATLAB* software and the respective code can be consulted in page 63.

Starting with the baseline geometry (30°), the wing displays a change in downforce of ±3% from the mean value, with a dominant frequency of around 8Hz, as seen in the FFT plot (Figure 30 (a)). Similar to the other two geometries, this is caused by the lower edge vortex fluctuations underneath the wing, as seen in the previous section of this work. As for drag, the wing is seen to be slightly more affected, experiencing a variation ranging from −4.5% to +3.5%. Concerning the AOA of 32°, the FFT plot (Figure 30 (b)) shows a dominant frequency of 24Hz, with a change in downforce ranging from −4.5% to +1.3%. In contrast to the baseline geometry, the drag force is now significantly more affected, observing a variation that ranges from −8% to +4%. Finally, regarding the 34° flap configuration, the FFT plot (Figure 30 (c)) shows a dominant frequency of 13Hz, with an extra significant peak at around 36Hz. The downforce on the wing varies from −3% to +5%, while the drag ranges from −7% to +4.5%, once again being more affected when compared to the baseline geometry. Seeing that the vortex breakdown is located near the wing's trailing edge might explain this occurrence [27], that is to say why higher drag force fluctuations are observed, relative to downforce variations, in all three configurations. The Reynolds Number translates the relative importance of viscous versus pressure drag. At high Reynolds numbers such as this study, pressure drag dominates, so the most effective way of reducing drag is to reduce the size of the low-pressure wake [39]. Therefore, observing a large recirculation zone at the trailing edge of the wing is synonym of a low pressure region wake and, consequently, increased pressure drag. Lastly, it remains important to mention that the upper edge vortex is stable in its development and for that reason will not significantly affect the forces acting on the wing.

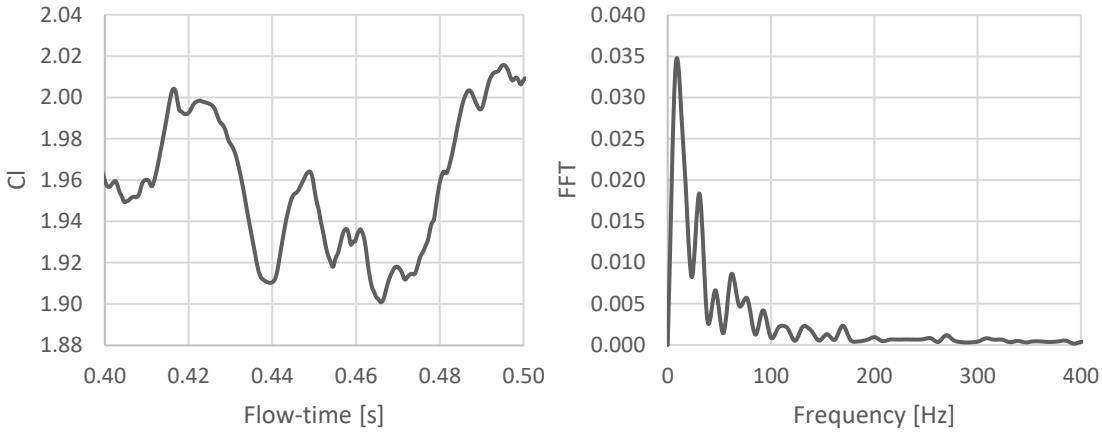

(a) AOA of 30 degrees

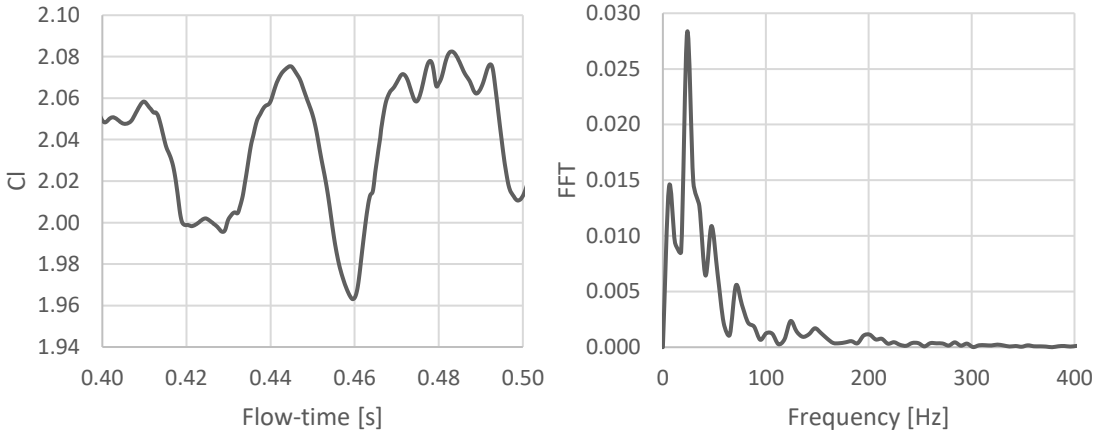

(b) AOA of 32 degrees

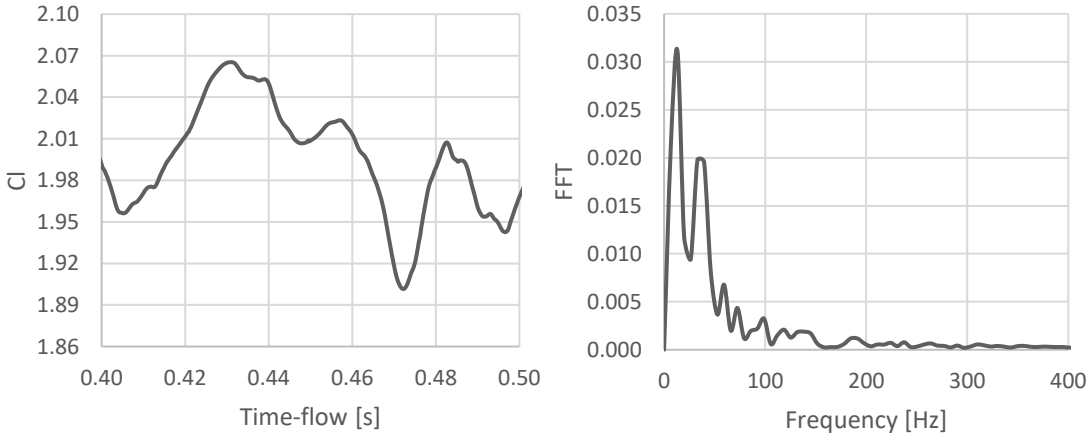

(c) AOA of 34 degrees

Figure 30 - Variation with time and Fast Fourier Transform of the wing downforce coefficient for (a) AOA of 30 degrees, (b) AOA of 32 degrees and (c) AOA of 34 degrees.

Chapter 4

Conclusion

The present and final chapter serves as a summary of all the relevant information acquired during the numerical study presented in this thesis, regarding the wing-wheel flow interaction and its effect on the underbody's feeding process. Then, to conclude, some comments will be made regarding future work suggestions, bearing in mind the difficulties and possible errors made throughout the whole process.

A numerical study using a DES approach concerning the aerodynamics of an inverted three-element wing and wheel was done. Following an analysis of the data collected, one can remark the following conclusions:

1. Lacking a CFD study in order to optimize the modelled wing and confirming initial worries, vortex breakdown does indeed occur to the lower edge vortex, located underneath the wing. Such is the case for all three geometries investigated. The breakdown is believed to occur as a consequence of the lower edge vortex produced being too weak to sustain flow development. This has significant implications on the wing's performance, seeing that vortex breakdown is one of the primary downforce limiting mechanisms. Further downstream, wheel wake management is also impaired, as only a coherent vortex could significantly affect and laterally contain the wake coming from the wheel.

2. The angle of attack of the second flap has little to no influence on the upper edge vortex. Reason for this is that the pressure increase provided by the stagnation point at the most upstream location of the wheel is greater than that which may be obtained by increasing the angle of attack.

3. Concerning a rotating wheel in a moving ground, a lower turbulent flow to the side of the wheel, where the tyre meets the road, was expected and this was observed in all three configurations. Compared to the baseline geometry, the 32 and 34 degrees configurations exhibit a more confined turbulent flow, although the latter being less vertically restrained. This is believed to happen because the baseline geometry sees the most disturbed flow succeeding vortex breakdown and, as a consequence, its effectiveness on constraining the jetting effect becomes impaired.

4. The wheel wake can be divided into an upper and a lower wake. When comparing them both, the lower wheel wake extends further downstream, which is explained by the ground presence and jetting effect occurring between the tyre and the ground.

5. At the plane placed where the intake of the underbody would be, the wake coming from the wheel for both the 30 and 32 degrees configurations is generally about the same size, with the latter seeing the lower wake disrupting the area of intake more. Regarding the 34 degrees configuration, the wake structure is wider but significantly shorter and located more to the side. This structure displays more areas of low energy flow, indicating the resulting flow has a lot less energy than the other two. The increased downwash experienced in the central region of the wheel for this geometry is the explanation for this occurrence.

6. Looking at the streamwise velocity at the plane behind the wheel, the wake shows a very similar structure between the 30 and 32 degrees configurations, both exhibiting areas of strong reversed flow, which are contained within the profile of the tyre. Further downstream, a similar behaviour is observed, however the strong reversed flow regions are no longer present. The containment of the wake structure within the profile may be the explanation to this lack of advection of the reversed flow downstream of the wheel. The same cannot be said about the 34 degrees configuration, where the wake is shorter but wider at ground level, resembling more an inverted-T shape.

7. Analysing the vertical velocity plot at the plane behind the wheel, the 34 degrees configuration exhibits a fairly large area of downwash behind the central region of the wheel, unlike the other two geometries. This goes to justify what was seen in the streamwise velocity analysis because, as the separation point moves rearwards, the downwash generated in the central region of the wheel wake increases incrementally, leading to a resultant wheel wake that is shorter and further apart. The delay of the separation point is explained by the more aggressive flap configuration (AOA of 34 degrees) which induces more upwash, thus providing the boundary layer with more energy to overcome the adverse pressure region on top of the tyre.

8. After analysing the forces acting on the wing and their respective oscillations, a pattern across all three configurations can be identified – higher drag force fluctuations are observed, compared to downforce variations. This occurrence was attributed to the vortex breakdown (i.e., region of instability) location being near the wing's trailing edge. Lastly, one could also observe that the upper edge vortex is stable in its development and for that reason does not significantly affect the forces at play.

4.1. Future Work

The geometry used in this study is a simplified version of what can be seen in a Formula One racing car. This was done in order to restrict the number of complex components in what is already an intricate model, so that only the main flow features would play a role in the simulations. If a more realistic study was to be carried out, all components need to be analysed with no

exception – brake ducts, suspension arms, wheel fairings, tyre deflectors, etc. – for a thorougher experiment, considering all flow features and their interactions with one another. This is especially true concerning the tyre deflectors because their goal is to help manage the front wheel wake by cleaning up the airflow passing over the tyre, significantly affecting flow development and, consequently, the results.

A mesh independence study was performed analysing only the effects on force coefficient values. The solution was considered mesh independent once said values did not differ more than 1 to 2% for a higher mesh density. However, other aspects such as vortex behaviour have not been verified, so one might ponder if a higher mesh density would better predict the interactions among vortical structures in the flow. It is important to mention that mesh density was limited to time restraints, as each configuration took already close to 15 days to simulate. Finally, obtaining a correct set of y^+ values was favoured to the detriment of some boundary layer resolution, so that the turbulence model requirements were met, without exceeding a reasonable time frame.

Higher computational resources could allow the application of more demanding numerical methods (i.e., turbulence models), perhaps improving the fidelity of the tests. Therefore, it could be interesting to develop a study where one tried to assess to what extent the application of a demanding model becomes beneficial, justifying both higher costs and higher running times.

The angle of attack of the second flap was the only parameter varied in this study, with ride height and flap geometry remaining constant. The latter is especially relevant, because as it was observed in the flow analysis section, vortex breakdown does occur. If an optimization process of the elements present on the wing were to be put in place, undesirable phenomena such as this would be mitigated. Additional configurations could be tested such as changing the position of the wing relative to the wheel and varying the chord along the length of each flap.

Also relevant to mention is the fact that the endplate modelled in CAD is a very simplistic interpretation of the regulations. The main objective of this study was to analyse the implications that the AOA of the flap would impose on wheel wake aerodynamics. Therefore, the endplate was somewhat neglected and so were its implications on flow development. For this reason, one should be mindful of this aspect when interpreting the results.

The entire geometry was made from the ground up, thus making this model unique in any way, shape, or form. Hence, having no direct comparable data, neither experimental nor numerical, verification and validation of the results attained during this thesis was only made possible through a pressure coefficient study. A more appropriate way of verifying the validity of the simulations would be to run an experimental study alongside the numerical analysis, to perform data comparison.

“Racing cars are developed in different conditions to those experienced when on track following another car.” [40]. This is a fundamental issue experienced by most teams when racing their cars on track. The results attained in both experimental and computational simulations are for an

undisturbed, clean flow of air. One could suggest running the same experiments but in a tandem scenario, where a car follows another. This would be particularly interesting in accessing to what extent the new regulations worked as intended by the FIA.

Bibliography

[1] Wright, P. G. “Influence of Aerodynamics on the Design of Formula One Racing Cars.” International Journal of Vehicle Design, Vol. 3, No. 4, 1982, pp. 383–397. https://doi.org/10.1504/IJVD.1982.061285.

[2] Katz, J. “Aerodynamics of Race Cars.” Annual Review of Fluid Mechanics, 2006. https://doi.org/10.1146/annurev.fluid.38.050304.092016.

[3] Hucho, W.-H. Aerodynamics of Road Vehicles: From Fluid Mechanics to Vehicle Engineering - Chapter 8. 1987.

[4] Agathangelou, B., and Gascoyne, M. Aerodynamic Design Considerations of a Formula 1 Racing Car. 1998.

[5] Pegrum, J. M. Experimental Study of the Vortex System Generated by a Formula 1 Front Wing. Imperial College London, 2007.

[6] JEong, J., and Hussain, F. “On the Identification of a Vortex.” Journal of Fluid Mechanics, 1995. https://doi.org/10.1017/S0022112095000462.

[7] Green, S. I. Fluid Vortices - Chapter 1. 1995.

[8] Anderson, J. D. Fundamentals of Aerodynamics, 2nd Edition. 1991.

[9] Delery, J. M. “Aspects of Vortex Breakdown.” Progress in Aerospace Sciences, 1994, pp. 1–59. https://doi.org/10.1016/0376-0421(94)90002-7.

[10] Peckham, D. H., and Atkinson, S. A. Preliminary Results of Low Speed Wind Tunnel Tests on a Gothic Wing of Aspect Ratio 1.0. Royal Aircraft Establishment, 1957.

[11] Harvey, J. K. “Some Observations of the Vortex Breakdown Phenomenon.” Journal of Fluid Mechanics, 1962. https://doi.org/10.1017/S0022112062001470.

[12] Benjamin, T. B. “Theory of the Vortex Breakdown Phenomenon.” Journal of Fluid Mechanics, 1962. https://doi.org/10.1017/S0022112062001482.

[13] Leibovich, S. “Structure of Vortex Breakdown.” Annual Review of Fluid Mechanics, 1978. https://doi.org/10.1146/annurev.fl.10.010178.001253.

[14] Sarpkaya, T. “On Stationary and Travelling Vortex Breakdowns.” Journal of Fluid Mechanics, 1971. https://doi.org/10.1017/S0022112071000181.

[15] Sarpkaya, T. “Vortex Breakdown in Swirling Conical Flows.” AIAA Journal, 1971. https://doi.org/10.2514/3.49981.

[16] Faler, J. H., and Leibovich, S. “Disrupted States of Vortex Flow and Vortex Breakdown.” Physics of Fluids, 1977. https://doi.org/10.1063/1.862033.

[17] Lucca-Negro, O., and O’Doherty, T. “Vortex Breakdown: A Review.” Progress in Energy and Combustion Science, 2001. https://doi.org/10.1016/S0360-1285(00)00022-8.

[18] Leibovich, S. “Vortex Stability and Breakdown - Survey and Extension.” AIAA Journal, 1984. https://doi.org/10.2514/3.8761.

[19] Mercker, E., Breuer, N., Berneburg, H., and Emmelmann, H. J. On the Aerodynamic Interference Due to the Rolling Wheels of Passenger Cars. 1991.

[20] Fackrell; J. E. The Aerodynamics of an Isolated Wheel Rotating in Contact With the Ground. 1974.

[21] Hobeika, T., Sebben, S., and Landstrom, C. “Investigation of the Influence of Tyre Geometry on the Aerodynamics of Passenger Cars.” SAE International Journal of Passenger Cars - Mechanical Systems, 2013. https://doi.org/10.4271/2013-01-0955.

[22] Knowles, R. D. Monoposto Racecar Wheel Aerodynamics: Investigation of Near-Wake Structure and Support-Sting Interference. Cranfield University, 2007.

[23] Kellar, Pearse, and Savill. “Formula 1 Car Wheel Aerodynamics.” Sports Engineering, 1999. https://doi.org/10.1046/j.1460-2687.1999.00030.x.

[24] Diasinos, S., and Gatto, A. “Experimental Investigation into Wing Span and Angle-of-Attack Effects on Sub-Scale Race Car Wing/Wheel Interaction Aerodynamics.” Experiments in Fluids, 2008. https://doi.org/10.1007/s00348-008-0499-z.

[25] Van Den Berg, M. A. Aerodynamic Interaction of an Inverted Wing with a Rotating Wheel. PhD Thesis, University of Southampton, 2007.

[26] Van Den Berg, M. A., and Zhang, X. “The Aerodynamic Interaction between an Inverted Wing and a Rotating Wheel.” Journal of Fluids Engineering, Transactions of the ASME, 2009. https://doi.org/10.1115/1.3215942.

[27] Heyder-Bruckner, J. The Aerodynamics of an Inverted Wing and a Rotating Wheel in Ground Effect. PhD Thesis, University of Southampton, Engineering Sciences, 2011.

[28] Qu, Q., Zuo, P., Qin, Y., Liu, P., and Agarwal, R. K. Numerical Investigation of the Aerodynamics of an Inverted Three-Element Airfoil in Ground Effect for Race Car Application. Proceedings of the 34th AIAA Applied Aerodynamics Conference. 2016.

[29] Mahon, S. A. The Aerodynamics of Multi-Element Wings in Ground Effect. PhD Thesis, University of Southampton, 2005.

[30] ANSYS Fluent Tutorial Guide 18. 2018.

[31] Lanfrit, M. “Best Practice Guidelines for Handling Automotive External Aerodynamics with FLUENT.” 2005.

[32] Salim, S. M., and Cheah, S. C. Wall y + Strategy for Dealing with Wall-Bounded Turbulent Flows. Proceedings of the International MultiConference of Engineers and Computer Scientists (IMECS). 2009.

[33] Spalart, P. R., Jou, W. H., Strelets, M. K., and Allmaras, S. R. Comments on the Feasibility of LES for Wings and on a Hybrid RANS/LES Approach. First AFOSR International Conference on DNS/LES - Advances in DNS/LES. 1997.

[34] Javaherchi. “Review of Spalart-Allmaras Turbulence Model and Its Modifications.” University of Washington, 2010.

[35] Shur, M., Spalart, P. R., Strelets, M., and Travin, A. Detached-Eddy Simulation of an Airfoil at High Angle of Attack. 4th International Symposium on Engineering Turbulence Modelling and Experiments. 1999.

[36] Spalart, P. R., Deck, S., Shur, M. L., Squires, K. D., Strelets, M. K., and Travin, A. “A New Version of Detached-Eddy Simulation, Resistant to Ambiguous Grid Densities.” Theoretical and Computational Fluid Dynamics, 2006. https://doi.org/10.1007/s00162-006-0015-0.

[37] Diasinos, S. The Aerodynamic Interaction of a Rotating Wheel and a Downforce Producing Wing in Ground Effect. University of New South Wales, 2009.

[38] Knowles, R. D., Saddington, A. J., and Knowles, K. “On the near Wake of a Formula One Front Wheel.” Proceedings of the Institution of Mechanical Engineers, Part D: Journal of Automobile Engineering, 2013. https://doi.org/10.1177/0954407013491903.

[39] Alexander, D. E. Fluid Biomechanics. In Nature’s Machines, 2017.

[40] Correia, J., Roberts, L. S., Finnis, M. V., and Knowles, K. Aerodynamic Characteristics of a Monoposto Racing Car Front Wing Operating in High Turbulence Conditions. In The International Vehicle Aerodynamics Conference, 2014.

Appendix A

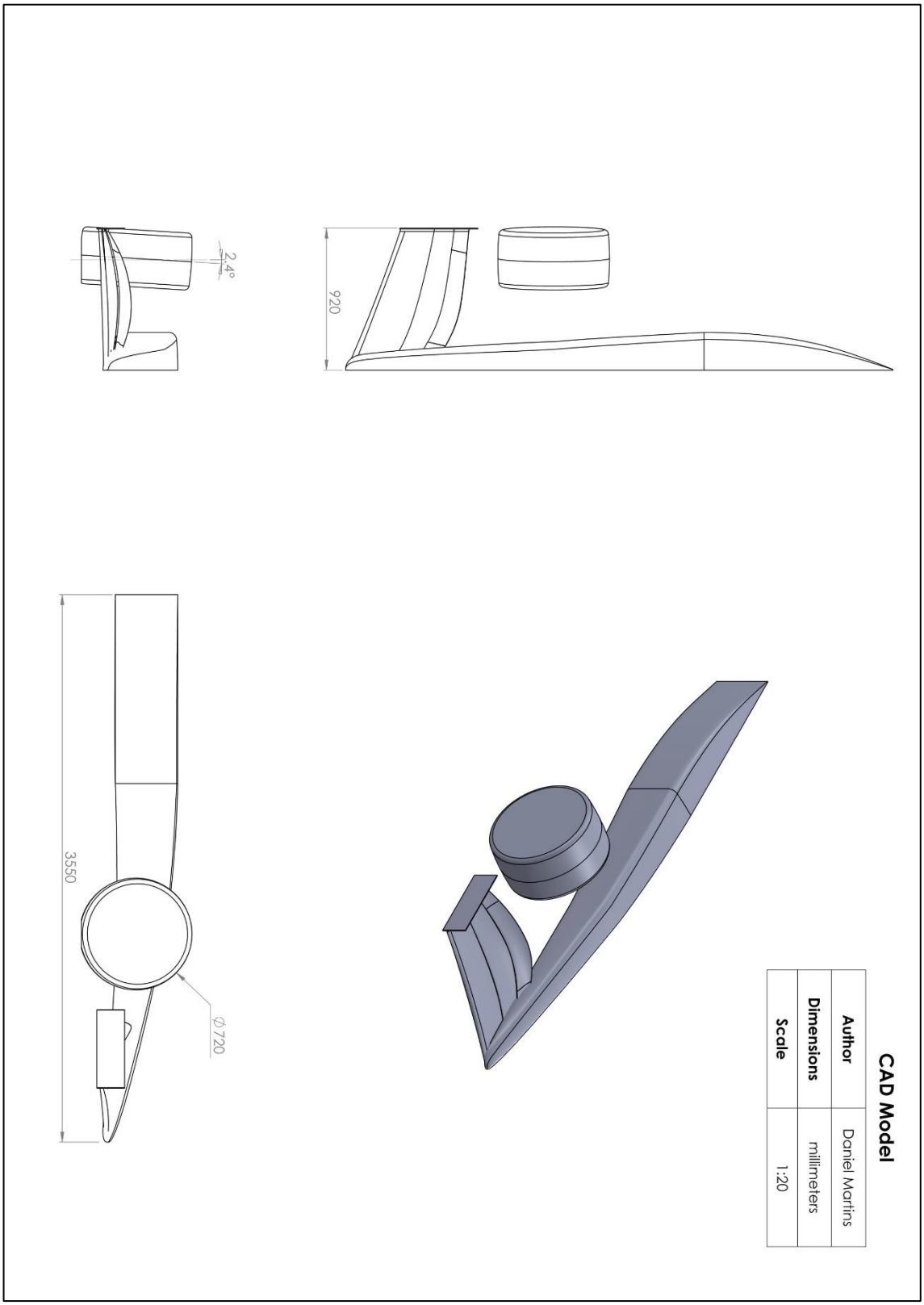
2.4°
920
3550
Ø 720
CAD Model
Author
Daniel Martins
Dimensions
millimeters
Scale
1:20

Appendix B

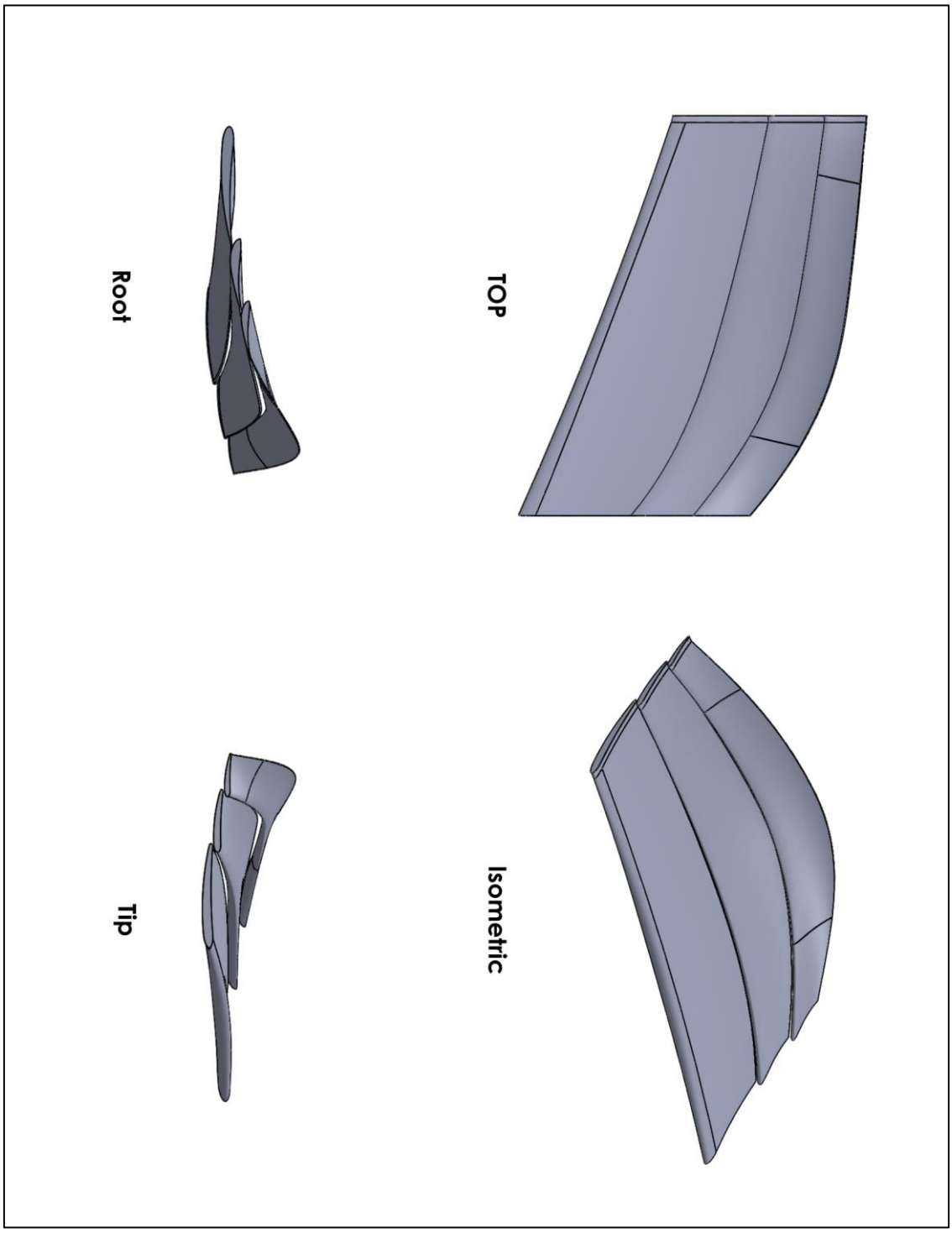

Appendix C

```
% Read Excel file

[D,S] = xlsread('filename.xlsx');

% FFT

t = D(:,1);
Cl = D(:,2);
Ts = mean(diff(t));
Fs = 1/Ts;
Fn = Fs/2;
L = numel(t);
Clm = Cl-mean(Cl);                                  % Subtract Mean (Mean = 0 Hz)
FCl = fft(Clm)/L;
Fv = linspace(0, 1, fix(L/2)+1)*Fn;
Iv = 1:numel(Fv);

% Find local maxima

[pks,locs] = findpeaks(abs(FCl(Iv))*2, 'MinPeakHeight',0.01);

% Plot graph

figure
plot(Fv, abs(FCl(Iv))*2)
grid
xlim([0 1E3])
text(Fv(locs), pks, sprintf('\\leftarrow Dominant Frequency = %.2f', Fv(locs)),
'HorizontalAlignment','left')

% Extract plot to text file

h = findobj(gca,'Type','line');
x=get(h,'Xdata');
y=get(h,'Ydata');
save('xfile.txt', 'x', '-ASCII','-append');
save('yfile.txt', 'y', '-ASCII','-append');
```

Appendix D

Main-Plate									Flap 1									Flap 2								
Root			Mid			Tip			Root			Mid			Tip			Root			Mid			Tip		
X	Y	Z	X	Y	Z	X	Y	Z	X	Y	Z	X	Y	Z	X	Y	Z	X	Y	Z	X	Y	Z	X	Y	Z
0.000	0.167	-0.100	-0.450	0.155	-0.191	-0.900	0.126	-0.353	0.000	0.186	-0.262	-0.450	0.181	-0.471	-0.900	0.145	-0.575	0.000	0.206	-0.404	-0.450	0.253	-0.635	-0.900	0.166	-0.703
0.000	0.169	-0.068	-0.450	0.161	-0.194	-0.900	0.128	-0.356	0.000	0.188	-0.263	-0.450	0.183	-0.472	-0.900	0.146	-0.576	0.000	0.208	-0.404	-0.450	0.322	-0.752	-0.900	0.167	-0.704
0.000	0.172	-0.043	-0.450	0.146	-0.194	-0.900	0.122	-0.356	0.000	0.182	-0.262	-0.450	0.178	-0.472	-0.900	0.143	-0.576	0.000	0.205	-0.404	-0.450	0.254	-0.635	-0.900	0.165	-0.704
0.000	0.172	-0.022	-0.450	0.139	-0.203	-0.900	0.130	-0.361	0.000	0.189	-0.268	-0.450	0.185	-0.477	-0.900	0.147	-0.578	0.000	0.208	-0.406	-0.450	0.251	-0.636	-0.900	0.164	-0.706
0.000	0.168	-0.008	-0.450	0.168	-0.204	-0.900	0.120	-0.361	0.000	0.176	-0.268	-0.450	0.173	-0.477	-0.900	0.142	-0.578	0.000	0.202	-0.406	-0.450	0.255	-0.637	-0.900	0.169	-0.709
0.000	0.163	-0.004	-0.450	0.170	-0.219	-0.900	0.131	-0.367	0.000	0.189	-0.276	-0.450	0.187	-0.483	-0.900	0.148	-0.582	0.000	0.209	-0.410	-0.450	0.249	-0.638	-0.900	0.164	-0.708
0.000	0.157	-0.007	-0.450	0.135	-0.217	-0.900	0.118	-0.367	0.000	0.171	-0.276	-0.450	0.170	-0.484	-0.900	0.141	-0.582	0.000	0.198	-0.410	-0.450	0.257	-0.639	-0.900	0.168	-0.706
0.000	0.152	-0.015	-0.450	0.134	-0.236	-0.900	0.131	-0.375	0.000	0.189	-0.287	-0.450	0.189	-0.490	-0.900	0.149	-0.586	0.000	0.209	-0.415	-0.450	0.248	-0.640	-0.900	0.163	-0.716
0.000	0.150	-0.024	-0.450	0.167	-0.237	-0.900	0.116	-0.375	0.000	0.168	-0.286	-0.450	0.168	-0.490	-0.900	0.140	-0.585	0.000	0.196	-0.413	-0.450	0.259	-0.643	-0.900	0.172	-0.793
0.000	0.147	-0.041	-0.450	0.165	-0.253	-0.900	0.131	-0.383	0.000	0.188	-0.297	-0.450	0.191	-0.498	-0.900	0.149	-0.589	0.000	0.204	-0.519	-0.450	0.247	-0.643	-0.900	0.169	-0.712
0.000	0.145	-0.067	-0.450	0.133	-0.252	-0.900	0.115	-0.383	0.000	0.166	-0.296	-0.450	0.167	-0.499	-0.900	0.140	-0.589	0.000	0.209	-0.419	-0.450	0.261	-0.648	-0.900	0.163	-0.712
0.000	0.144	-0.098	-0.450	0.132	-0.274	-0.900	0.130	-0.392	0.000	0.187	-0.307	-0.450	0.193	-0.506	-0.900	0.139	-0.595	0.000	0.194	-0.418	-0.450	0.247	-0.649	-0.900	0.169	-0.716
0.000	0.144	-0.125	-0.450	0.162	-0.275	-0.900	0.115	-0.391	0.000	0.165	-0.306	-0.450	0.167	-0.506	-0.900	0.149	-0.596	0.000	0.209	-0.423	-0.450	0.264	-0.653	-0.900	0.169	-0.722
0.000	0.146	-0.155	-0.450	0.160	-0.297	-0.900	0.130	-0.402	0.000	0.186	-0.319	-0.450	0.195	-0.516	-0.900	0.142	-0.656	0.000	0.193	-0.422	-0.450	0.247	-0.655	-0.900	0.163	-0.722
0.000	0.150	-0.191	-0.450	0.132	-0.297	-0.900	0.114	-0.402	0.000	0.165	-0.318	-0.450	0.168	-0.517	-0.900	0.150	-0.656	0.000	0.208	-0.428	-0.450	0.267	-0.660	-0.900	0.169	-0.726
0.000	0.155	-0.222	-0.450	0.158	-0.316	-0.900	0.129	-0.414	0.000	0.185	-0.332	-0.450	0.197	-0.526	-0.900	0.149	-0.602	0.000	0.191	-0.427	-0.450	0.248	-0.661	-0.900	0.163	-0.726
0.000	0.161	-0.251	-0.450	0.132	-0.318	-0.900	0.113	-0.414	0.000	0.166	-0.331	-0.450	0.169	-0.527	-0.900	0.139	-0.602	0.000	0.208	-0.434	-0.450	0.270	-0.665	-0.900	0.169	-0.731
0.000	0.166	-0.273	-0.450	0.157	-0.335	-0.900	0.128	-0.425	0.000	0.184	-0.344	-0.450	0.199	-0.536	-0.900	0.148	-0.607	0.000	0.190	-0.433	-0.450	0.250	-0.665	-0.900	0.163	-0.730
0.000	0.168	-0.273	-0.450	0.133	-0.337	-0.900	0.113	-0.424	0.000	0.168	-0.344	-0.450	0.171	-0.537	-0.900	0.139	-0.606	0.000	0.207	-0.442	-0.450	0.272	-0.671	-0.900	0.169	-0.734
0.000	0.166	-0.251	-0.450	0.156	-0.353	-0.900	0.128	-0.436	0.000	0.184	-0.355	-0.450	0.201	-0.546	-0.900	0.148	-0.612	0.000	0.190	-0.441	-0.450	0.252	-0.672	-0.900	0.163	-0.734
0.000	0.165	-0.221	-0.450	0.134	-0.353	-0.900	0.113	-0.436	0.000	0.170	-0.355	-0.450	0.174	-0.546	-0.900	0.139	-0.612	0.000	0.206	-0.450	-0.450	0.276	-0.677	-0.900	0.169	-0.739
0.000	0.164	-0.189	-0.450	0.135	-0.368	-0.900	0.127	-0.446	0.000	0.184	-0.365	-0.450	0.202	-0.554	-0.900	0.148	-0.619	0.000	0.190	-0.448	-0.450	0.256	-0.679	-0.900	0.163	-0.739
0.000	0.165	-0.126	-0.450	0.156	-0.368	-0.900	0.113	-0.446	0.000	0.172	-0.365	-0.450	0.178	-0.555	-0.900	0.139	-0.619	0.000	0.206	-0.457	-0.450	0.278	-0.683	-0.900	0.170	-0.743
0.000	0.164	-0.155	-0.450	0.156	-0.384	-0.900	0.127	-0.457	0.000	0.184	-0.374	-0.450	0.204	-0.562	-0.900	0.148	-0.626	0.000	0.191	-0.455	-0.450	0.260	-0.685	-0.900	0.164	-0.744
0.000	0.171	-0.015	-0.450	0.137	-0.383	-0.900	0.113	-0.456	0.000	0.174	-0.374	-0.450	0.181	-0.562	-0.900	0.139	-0.626	0.000	0.205	-0.464	-0.450	0.281	-0.689	-0.900	0.170	-0.748
0.000	0.148	-0.030	-0.450	0.156	-0.405	-0.900	0.127	-0.467	0.000	0.184	-0.383	-0.450	0.206	-0.570	-0.900	0.149	-0.632	0.000	0.192	-0.463	-0.450	0.263	-0.690	-0.900	0.164	-0.748
0.000	0.173	-0.031	-0.450	0.140	-0.404	-0.900	0.113	-0.467	0.000	0.176	-0.383	-0.450	0.185	-0.570	-0.900	0.140	-0.632	0.000	0.205	-0.471	-0.450	0.285	-0.696	-0.900	0.170	-0.753

0.000	0.171	-0.055	-0.450	0.156	-0.422	-0.900	0.127	-0.482	0.000	0.185	-0.390	-0.450	0.208	-0.578	-0.900	0.149	-0.640	0.000	0.193	-0.470	-0.450	0.269	-0.697	-0.900	0.165	-0.753
0.000	0.145	-0.055	-0.450	0.142	-0.421	-0.900	0.113	-0.482	0.000	0.178	-0.390	-0.450	0.189	-0.580	-0.900	0.140	-0.640	0.000	0.205	-0.478	-0.450	0.288	-0.702	-0.900	0.170	-0.757
0.000	0.169	-0.012	-0.450	0.157	-0.435	-0.900	0.127	-0.497	0.000	0.186	-0.396	-0.450	0.211	-0.590	-0.900	0.149	-0.648	0.000	0.194	-0.478	-0.450	0.273	-0.703	-0.900	0.165	-0.757
0.000	0.168	-0.080	-0.450	0.145	-0.435	-0.900	0.114	-0.496	0.000	0.179	-0.396	-0.450	0.195	-0.590	-0.900	0.141	-0.647	0.000	0.205	-0.485	-0.450	0.292	-0.709	-0.900	0.171	-0.762
0.000	0.144	-0.080	-0.450	0.157	-0.444	-0.900	0.127	-0.511	0.000	0.186	-0.402	-0.450	0.214	-0.599	-0.900	0.152	-0.712	0.000	0.196	-0.485	-0.450	0.279	-0.710	-0.900	0.166	-0.762
0.000	0.166	-0.111	-0.450	0.147	-0.443	-0.900	0.115	-0.510	0.000	0.181	-0.402	-0.450	0.200	-0.599	-0.900	0.155	-0.711	0.000	0.205	-0.491	-0.450	0.295	-0.714	-0.900	0.171	-0.766
0.000	0.144	-0.111	-0.450	0.158	-0.455	-0.900	0.127	-0.522	0.000	0.187	-0.406	-0.450	0.217	-0.610	-0.900	0.150	-0.665	0.000	0.197	-0.491	-0.450	0.283	-0.714	-0.900	0.166	-0.766
0.000	0.167	-0.089	-0.450	0.149	-0.457	-0.900	0.117	-0.521	0.000	0.182	-0.406	-0.450	0.205	-0.610	-0.900	0.143	-0.666	0.000	0.205	-0.496	-0.450	0.298	-0.719	-0.900	0.172	-0.771
0.000	0.144	-0.088	-0.450	0.158	-0.465	-0.900	0.128	-0.532	0.000	0.188	-0.410	-0.450	0.220	-0.617	-0.900	0.151	-0.673	0.000	0.198	-0.496	-0.450	0.288	-0.720	-0.900	0.167	-0.771
0.000	0.164	-0.141	-0.450	0.151	-0.466	-0.900	0.118	-0.533	0.000	0.184	-0.410	-0.450	0.210	-0.618	-0.900	0.144	-0.674	0.000	0.206	-0.502	-0.450	0.302	-0.725	-0.900	0.172	-0.775
0.000	0.145	-0.141	-0.450	0.159	-0.475	-0.900	0.120	-0.546	0.000	0.187	-0.416	-0.450	0.223	-0.624	-0.900	0.151	-0.682	0.000	0.200	-0.502	-0.450	0.294	-0.726	-0.900	0.168	-0.775
0.000	0.164	-0.173	-0.450	0.154	-0.475	-0.900	0.128	-0.545	0.000	0.188	-0.414	-0.450	0.214	-0.625	-0.900	0.145	-0.682	0.000	0.206	-0.509	-0.450	0.306	-0.731	-0.900	0.172	-0.779
0.000	0.148	-0.174	-0.450	0.160	-0.483	-0.900	0.129	-0.556	0.000	0.185	-0.414	-0.450	0.226	-0.632	-0.900	0.152	-0.688	0.000	0.202	-0.509	-0.450	0.299	-0.732	-0.900	0.169	-0.780
0.000	0.164	-0.205	-0.450	0.156	-0.483	-0.900	0.121	-0.557	0.000	0.187	-0.262	-0.450	0.219	-0.633	-0.900	0.147	-0.689	0.000	0.207	-0.514	-0.450	0.310	-0.736	-0.900	0.173	-0.784
0.000	0.152	-0.205	-0.450	0.160	-0.489	-0.900	0.130	-0.569	0.000	0.184	-0.262	-0.450	0.230	-0.640	-0.900	0.153	-0.695	0.000	0.203	-0.514	-0.450	0.304	-0.737	-0.900	0.170	-0.784
0.000	0.166	-0.236	-0.450	0.157	-0.489	-0.900	0.123	-0.568	0.000	0.189	-0.265	-0.450	0.223	-0.640	-0.900	0.148	-0.695	0.000	0.208	-0.519	-0.450	0.315	-0.742	-0.900	0.174	-0.789
0.000	0.157	-0.236	-0.450	0.159	-0.490	-0.900	0.130	-0.575	0.000	0.179	-0.265	-0.450	0.232	-0.646	-0.900	0.154	-0.703	0.000	0.208	-0.523	-0.450	0.310	-0.742	-0.900	0.171	-0.790
0.000	0.167	-0.261	-0.450	0.164	-0.197	-0.900	0.124	-0.576	0.000	0.189	-0.273	-0.450	0.227	-0.646	-0.900	0.149	-0.703	0.000	0.206	-0.523	-0.450	0.318	-0.746	-0.900	0.174	-0.793
0.000	0.163	-0.261	-0.450	0.144	-0.196	-0.900	0.131	-0.582	0.000	0.174	-0.272	-0.450	0.236	-0.652	-0.900	0.154	-0.707	0.000	0.211	-0.533	-0.450	0.314	-0.746	-0.900	0.175	-0.796
0.000	0.154	-0.011	-0.450	0.158	-0.192	-0.900	0.126	-0.582	0.000	0.189	-0.282	-0.450	0.231	-0.652	-0.900	0.150	-0.707	0.000	0.209	-0.533	-0.450	0.321	-0.749	-0.900	0.172	-0.796
0.000	0.165	-0.005	-0.450	0.149	-0.192	-0.900	0.129	-0.590	0.000	0.169	-0.281	-0.450	0.203	-0.605	-0.900	0.154	-0.717	0.000	0.210	-0.534	-0.450	0.318	-0.750	-0.900	0.175	-0.799
0.000	0.160	-0.005	-0.450	0.169	-0.208	-0.900	0.131	-0.588	0.000	0.186	-0.313	-0.450	0.216	-0.604	-0.900	0.155	-0.715	0.000	0.209	-0.527	-0.450	0.307	-0.740	-0.900	0.173	-0.799
0.000	0.167	-0.274	-0.450	0.137	-0.207	-0.900	0.127	-0.588	0.000	0.164	-0.312	-0.450	0.235	-0.655	-0.900	0.153	-0.716	0.000	0.207	-0.527	-0.450	0.312	-0.739	-0.900	0.174	-0.800